Nuclear resonant spectroscopy

2004 J. Phys.: Condens. Matter 16 S497

(http://iopscience.iop.org/0953-8984/16/5/009)

INSTITUTE OF PHYSICS PUBLISHING JOURNAL OF PHYSICS: CONDENSED MATTER

J. Phys.: Condens. Matter **16** (2004) S497–S530 PII: S0953-8984(04)69423-9

Nuclear resonant spectroscopy

Wolfgang Sturhahn

Advanced Photon Source, Argonne National Laboratory, IL 60439, USA

E-mail: sturhahn@anl.gov

Received 22 September 2003
Published 23 January 2004
Online at stacks.iop.org/JPhysCM/16/S497 (DOI: 10.1088/0953-8984/16/5/009)

Abstract

Nuclear resonant scattering techniques with synchrotron radiation (SR) are introduced on a basic level. We focus on the theoretical background and on experimental aspects of two popular methods with a widening range of applications, nuclear resonant inelastic x-ray scattering and synchrotron Mössbauer spectroscopy. The inelastic method provides specific vibrational information, e.g., the phonon density of states. The Mössbauer method permits determination of hyperfine interactions. All nuclear resonance techniques take full advantage of the unique properties of SR: intensity, collimation, time structure, and polarization. As a result both methods discussed here have led to novel applications for materials under extreme conditions, proteins with biological functionality, and magnetic nanostructures.

(Some figures in this article are in colour only in the electronic version)

1. Introduction

This contribution provides an introduction to nuclear resonant scattering (NRS) techniques, which have become useful during the past decade at highly brilliant synchrotron radiation (SR) facilities. Practical importance has been achieved by nuclear resonant inelastic x-ray scattering (NRIXS) for the study of lattice dynamics and by synchrotron Mössbauer spectroscopy (SMS) for the study of hyperfine interactions. In brief, SMS includes scattering processes that occur without recoil, i.e., without participation of lattice vibrations, whereas NRIXS techniques use the possibility of simultaneous excitation of nuclear resonance and lattice vibrations. A comprehensive overview of the field has been given recently in a collection of review articles edited by Gerdau and de Waard [1].

The development of the synchrotron branch of NRS techniques was sparked by the pioneering experimental work of Gerdau *et al* [2] exploring the original proposal of Ruby [3]. These early experiments strongly suggested that SR experiments with nuclear resonances would greatly benefit from a new time-resolved technique instead of the energy-resolved measurements familiar from traditional Mössbauer spectroscopy. This novel approach resulted

from the particular properties of SR, which is emitted as sequence of very short x-ray pulses of typically less than 100 ps duration. Energy spectroscopy in the microelectronvolts to nanoelectronvolts range is possible by analysis of the time decay pattern of x-rays scattered off or transmitted through samples containing a suitable nuclear resonant isotope. The measurement and analysis of such time spectra constitutes the main part of the SMS method. During the last decade, we have experienced the refinement of the SMS technique for obtaining hyperfine parameters, and applications in the areas of high-pressure research [4–8], thin-film and nanostructure magnetism [9–20], and biophysics research [21–27] have demonstrated its usefulness.

Conventional Mössbauer spectroscopy, like SMS, is based on the often appreciable probability that the resonant nuclei absorb x-rays without participation of lattice vibrations, i.e., are recoilless. But besides the extension of Mössbauer spectroscopy into the time domain, the construction of more powerful SR sources enabled NRS to establish a stronghold in a quite different area of condensed-matter physics: the determination of the phonon density of states (PDOS). The theoretical groundwork for this exciting opportunity was prepared early [28, 29], and demonstration experiments were carried out using strong radioactive sources that were tuned by large Doppler shifts [30, 31]. This direct approach was plagued by practical limitations caused by the notoriously small inelastic absorption cross section that had to be discerned against an overwhelmingly large background signal. These early experiments were almost forgotten when the idea of using nuclear resonances to observe phonon excitations was reborn in experiments by Seto *et al* [32] and others [33, 34], which used pulsed SR and a time-discrimination technique to circumvent the background problem. With these important ingredients, the NRIXS method started to produce unique results. The PDOS is an important quantity for describing the low-energy collective states of solids and is used to calculate thermodynamic properties related to lattice vibrations. Experimentally the PDOS is often obtained indirectly, e.g., by calculation from the phonon dispersion relations measured for single crystals using inelastic neutron scattering. The NRIXS technique provides direct access to the partial and projected PDOS of the resonant isotope only [35, 36]. The apparent disadvantage of being restricted to vibrational information from a few nuclear resonant isotopes has led to several unique applications. The most suitable nuclear resonant isotope is ^{57}Fe, and iron-containing materials, molecules, and proteins are of tremendous interest in geophysics, thin-film research, and biophysics. The NRIXS signals originate from particular nuclei only, and this complete isotope selectivity is truly unique among techniques for the study of lattice vibrations. For example, materials surrounding the sample that do not contain resonant nuclei produce no unwanted background, and this feature permitted high-pressure experiments in the Mbar regime that were impossible before [37–40]. Many proteins contain only a few iron atoms at their biologically active sites; NRIXS studies were conducted on several model compounds for such proteins [41–45], as well as on the proteins themselves [46–50]. Among the thousands of atoms, NRIXS selects only the iron vibrations and thus permits detailed studies of protein dynamics related to active sites. Similar reasoning applies to NRIXS studies of thin films or buried interfaces [51–57]. For buried interfaces, NRIXS may very well be the only technique able to obtain data on the vibrations. Also for nanoparticles [58–61] and disordered alloys [62, 63], the NRIXS method has been applied very successfully. In those cases, as well as for amorphous materials, phonon dispersions are difficult or impossible to measure and the vibrational density of states (DOS) gives valuable and often completely adequate information.

The development of NRS techniques was initially driven by an exploratory spirit, and eventually innovative SR instrumentation largely led to the success of SMS and NRIXS. The crucial new components were avalanche photo-diode (APD) detectors (reviewed by Baron [64]), for timing discrimination and the collection of time-resolved decay spectra, and

efficient and tunable high-energy-resolution monochromators (reviewed by Toellner [65]). The requirements of these two key components are somewhat different for SMS or NRIXS and are imposed by the different natures of the scattering processes as described later. For NRIXS, the monochromator must be tunable around the nuclear transition energy in a range comparable to that of vibrational excitations, typically a fraction of an electronvolt. The energy resolution achieved is determined by the bandwidth of the x-rays, typically of the order of 1 meV. In the case of SMS, tunability is not as crucial as stability because the monochromator must provide a high spectral intensity at the nuclear transition energy. The APD detector should cover a large solid angle with reasonable efficiency for NRIXS measurements. For SMS, the APD detector only needs to cover the size of the x-ray beam, and smaller devices with better timing characteristics can be used. A time resolution of a nanosecond or better and a very large dynamic range of nine orders of magnitude is typically needed for both techniques. The factual importance of instrumentation development notwithstanding, x-ray optics and detectors will not be discussed in any detail in this paper.

2. Basics on nuclear resonances

Standard textbooks on experimental techniques with SR discuss mechanisms that are based on the scattering of x-rays by electronic charge and spin. An argument from classical electrodynamics usually provides the justification for ignoring the nuclear charge. The Thomson-scattering cross section for electromagnetic radiation by a point charge q with mass m is given by

$$\sigma_{\mathrm{T}} = \frac{8\pi}{3}\left(\frac{q^2}{mc^2}\right)^2. \tag{1}$$

The scattering strength of the nucleus compared to the electron shell is then reduced by a factor $(Zm/M)^2 \approx 10^{-7}$, where m, M are the masses of the electron and nucleus, and Z is the atomic number. In this long-wavelength limit, which is justified for x-rays, the nuclear charge scattering is reduced by orders of magnitude because of the large nuclear mass, and it seems completely appropriate to ignore scattering contributions from the nucleus. However, the above argument fails if the timescale of internal nuclear dynamics matches the energy of the x-ray photon, i.e., the nucleus experiences a resonant excitation. The nuclear resonant cross section is then calculated as

$$\sigma_{\mathrm{N}} = \frac{\lambda^2}{2\pi}\frac{1}{1+\alpha}\frac{2I'+1}{2I+1}, \tag{2}$$

where λ is the wavelength of the resonant x-rays, α is the internal conversion coefficient, and I, I' are the spins of the nuclear ground and excited state. The probability that an excited nucleus directly transfers its excess energy to the electron shell and that this is followed by expulsion of an inner electron is given by $\alpha/(1+\alpha)$. Values of α for relevant nuclear transitions range from 1 to 1000. The nuclear resonant cross section can become very large, e.g., the 14.4 keV nuclear transition of ^{57}Fe gives with $\lambda = 86$ pm, $\alpha = 8.6$, $I = 1/2$, $I' = 3/2$ a value of $\sigma_{\mathrm{N}} = 2.56$ Mb and a ratio $\sigma_{\mathrm{N}}/\sigma_{\mathrm{T}} \approx 5700$. It should be noted that the photoelectric cross section often exceeds σ_{T}, but we still observe $\sigma_{\mathrm{N}}/\sigma_{\mathrm{pe}} \approx 450$. Naturally the question arises as to why NRS has taken a back seat compared to other popular x-ray scattering methods. Even though the nuclear resonant cross section is very large, the energy width of such resonances is very narrow. The weakness of the nuclear coupling to its electronic surroundings and to the electromagnetic field results in a weakly damped resonance of high quality, e.g., the energy width of the ^{57}Fe resonance is only $\Gamma = 4.66$ neV. Such extraordinarily narrow resonances escape detection by traditional x-ray scattering methods because the best energy resolutions of x-ray optics are

Table 1. List of isotopes with nuclear transitions below 30 keV that are feasible for NRS experiments. The transition energy is E_0, and τ is the lifetime of the excited nuclear state. The fourth column gives the strength of the nuclear response under optimal conditions. The strength for each isotope is estimated by $\Gamma\sigma_N/\sigma_{pe}$ and then divided by the value for ^{57}Fe, where σ_N is the nuclear resonant cross section, Γ is the width of the excited nuclear state, and σ_{pe} is the photoelectric cross section.

Isotope	E_0 (keV)	τ (ns)	Strength	First observation
^{181}Ta	6.214	8730	0.000 7	1995 [67]
^{169}Tm	8.410	5.8	0.38	1991 [68]
^{83}Kr	9.404	212	0.2	1995 [69]
^{73}Ge	13.263	4260	0.000 03	—
^{57}Fe	14.4125	141	1	1985 [2]
^{151}Eu	21.541	14	0.63	1996 [70]
^{149}Sm	22.496	10.2	1.3	2000 [71]
^{119}Sn	23.88	25.7	6.7	1993 [72]
^{161}Dy	25.651	40.5	1.2	1996 [73]
^{40}K	29.83	6.1	391	2000 [74]

in the 100 μeV regime [66]. A resonant enhancement over a nanoelectronvolt scale remains unresolved and unnoticed because even an experiment with bandwidth $\delta E \approx 100$ μeV would find $\sigma_N\Gamma \ll \sigma_{pe}\,\delta E$.

NRS techniques are nevertheless possible in the light of the inverse relationship between the nuclear level width and the lifetime of the nuclear state $\tau\Gamma = \hbar$. The value of τ determines the timescale on which a sample containing resonant nuclei would respond to an excitation by a SR pulse. For the ^{57}Fe resonance mentioned above, one obtains $\tau = 141$ ns. All electronic scattering of x-rays occurs typically on the timescale of femtoseconds, virtually immediate compared to nuclear resonant contributions. This mismatch leads us to the 'time-discrimination trick', which is illustrated in figure 3, and we understand how nuclear resonant signals are cleanly separated from other scattering contributions. In table 1, we show a list of nuclear isotopes that possess resonances below 30 keV. Higher transition energies are usually less favourable because the intensity of SR sources typically decreases with increasing x-ray energy, and x-ray optics, as well as detectors, become less efficient at higher energies.

3. Scattering processes

For a good understanding of NRIXS and SMS results, a study of the underlying scattering processes is required. Figure 1 summarizes the classification of elastic–inelastic and coherent–incoherent scattering processes, which is based on the analysis of the initial and final quantum states of the scatterer. The scattering process is symbolically expressed by

$$|\Phi_i\rangle|\gamma_i\rangle \longrightarrow |\Phi_n\rangle \longrightarrow |\Phi_f\rangle|\gamma_f\rangle, \tag{3}$$

where $|\gamma\rangle$ and $|\Phi\rangle$ describe states of the x-ray field and the scatterer, respectively, and the intermediate state does not contain x-ray photons. The inelastic scattering process is characterized by different energies of initial and final photon states. Thereby an energy transfer to the scatterer takes place. A meaningful definition of coherent and incoherent scattering is more sophisticated. The terminology usually intends to categorize the behaviour of a collection of atoms, for which we may write

$$|\Phi_i\rangle = |\chi_i\rangle \prod_j |\phi_i^{(j)}\rangle. \tag{4}$$

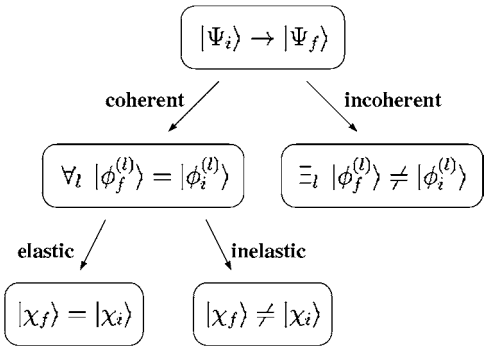

Figure 1. The classification scheme for scattering processes. The classification is based on initial and final quantum states of the scatterer. Incoherent scattering implies energy transfer to the photon field unless some core states are degenerate.

Here $|\phi^{(j)}\rangle$ symbolizes a core state, i.e., the state of the nucleus and inner electron shell, of atom j. The collective state of itinerant electrons and lattice vibrations is given by $|\chi\rangle$. Scattering processes that leave all core states $|\phi^{(j)}\rangle$ unchanged are called coherent because which atom scattered the photon cannot be decided. The change of just one atom's state serves as an indicator for local scattering and the process is called incoherent as illustrated in figure 1. In particular, SMS is based on the coherent elastic process, whereas NRIXS originates from incoherent processes. Coherent inelastic scattering by resonant nuclei has been shown to be of negligible strength in previous work [36]. The almost purely incoherent character of inelastic NRS simplifies the interpretation of NRIXS data and presents a clear distinction from inelastic neutron scattering where incoherent and coherent processes occur simultaneously. We may be concerned about the influence of inelastic coherent scattering by electronic charge on NRIXS because second-order processes involving coherent elastic NRS are difficult to estimate quantitatively. A detailed analysis of this problem has demonstrated however that such contaminating processes are of negligible effect [75].

4. NRIXS

The first part of this section will explain the principles of NRIXS and essentially answer the question of how nuclear resonances and lattice vibrations are related. We then continue to calculate the scattering cross section in a simplified form and explain the measurement process. The third part is dedicated to data interpretation including the extraction of the vibrational DOS.

4.1. Principles

The understanding of NRS is much simplified by the ratios of the energy scales involved:

$$\text{transition energy (keV)} \longleftrightarrow \text{phonon energy (meV)} \longleftrightarrow \text{nuclear level width (neV)}. \tag{5}$$

The energies are different by six orders of magnitude. Figure 2 illustrates this peculiar situation exemplified in more detail with the ^{57}Fe isotope. In panel (a), the ^{57}Fe nucleus is held fixed and is thus unable to dissipate any recoil energy. If we investigated this system with monochromatic x-rays, we would observe a sharp increase in cross section at the nuclear transition energy. The width of this Lorentzian response would be the nuclear level width Γ. For the 14.4 keV transition of ^{57}Fe, Γ is about 13 orders of magnitude smaller than the transition energy—a very

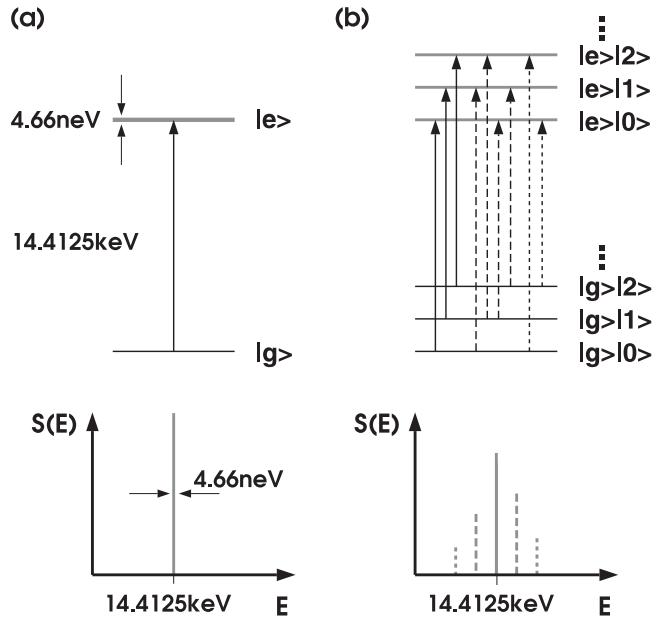

Figure 2. The influence of atomic vibration on the nuclear level scheme. Panel (a) shows the energy levels of a fixed ^{57}Fe nucleus. When x-rays interact with materials containing ^{57}Fe, the nuclear transition $|g\rangle \rightarrow |e\rangle$ causes a sharp resonance in the excitation probability density $S(E)$. The nucleus embedded in an Einstein solid has the more complex level scheme shown in panel (b). In addition to the peak at the nuclear transition energy, $S(E)$ now features sidebands. The dashed lines show transitions that include creation or annihilation of one phonon with the Einstein energy. Transitions that involve more phonons are also possible; e.g., the dotted lines describe two-phonon creation/annihilation. The strength of the vibration-coupled transitions of panel (b) is determined by the number of vibrational states at a particular energy (DOS) and their temperature-dependent occupation number.

narrow resonance indeed. Of course the notion of a 'fixed nucleus' is somewhat artificial, and one must consider a more realistic scenario. For a nucleus that is unbound and at rest relative to an observer, energy and momentum conservation result in a shift of the nuclear transition energy by

$$E_{\mathrm{R}} = \frac{E_0^2}{2Mc^2}, \tag{6}$$

where E_0 is the nuclear transition energy in the nuclear rest frame, and M is the mass of the nucleus. In the observer frame, the nuclear resonance is shifted upward by the 'recoil energy' E_{R}, which is invested in kinetic energy of the excited nucleus. For the 14.4 keV transition of ^{57}Fe, we calculate $E_{\mathrm{R}} = 1.956$ meV, a value that is much larger than the nuclear level width.

For the unbound nucleus, the absorption of the x-ray photon resulted in the *simultaneous* change of the nuclear state and quantum state of the centre of mass. The same ideas can be applied to understand the behaviour of bound nuclei, e.g., in solids. The absorption of the x-ray photon now leads to a simultaneous change of nuclear state and vibrational quantum state of the solid as illustrated in panel (b) of figure 2. New energy levels are created from combinations of nuclear states and phonon states; e.g., $|g\rangle|1\rangle$ is a quantum state with the nucleus in the ground state and one phonon present. The small coupling between the nucleus, phonon, and x-ray photon and the different energy scales mentioned before make such states very good approximations of the exact eigenstates of the coupled system. If we investigated

the vibrating nucleus with monochromatic x-rays, we would observe elastic transitions with energy E_0 of the type $|\mathrm{g}\rangle|n\rangle \longrightarrow |\mathrm{e}\rangle|n\rangle$, m-phonon creation of the type $|\mathrm{g}\rangle|n\rangle \longrightarrow |\mathrm{e}\rangle|n+m\rangle$ leading to upshifted transition energies $E_0 + m\epsilon$, and m-phonon annihilation of the type $|\mathrm{g}\rangle|n\rangle \longrightarrow |\mathrm{e}\rangle|n-m\rangle$ with $n \geqslant m$ leading to downshifted transition energies $E_0 - m\epsilon$. This behaviour is quantitatively described by the excitation probability density $S(E)$, and the cross section for a particular scattering channel is proportional to $S(E)$. The value of $S(E)\,\mathrm{d}E$ gives the probability that the nucleus can be excited by x-rays in the energy range $[E, E+\mathrm{d}E]$. The phonon creation/annihilation sidebands of $S(E)$ are conceptually equivalent to the Stokes and anti-Stokes lines of optical spectroscopies. The probability ratio $S(-E)/S(E)$ is universally given by the Boltzmann factor, i.e., $S(E) = \exp[E/k_\mathrm{B}T]S(-E)$ with temperature T and Boltzmann's constant k_B. This imbalance rule is known as 'detailed balance' and is an intrinsic feature of all NRIXS spectra. At zero temperature the effect is extreme because phonon annihilation becomes impossible, and $S(E)$ has only one sideband at positive energies.

4.2. Cross section and observation

Scattering probabilities have been calculated in a modern approach by Sturhahn and Kohn [36] using the Green function formalism. Here we will choose a simpler route to calculate the total nuclear absorption cross section, similar to that of Singwi and Sjölander [29]. We start with Fermi's golden rule which gives us the transition rate Λ_{ni} for the system changing from initial state $|\Phi_\mathrm{i}\rangle = |\chi_\mathrm{i}\rangle|\phi_\mathrm{i}\rangle$ to an intermediate state $|\Phi_n\rangle = |\chi_n\rangle|\phi_n\rangle$ under the influence of a monochromatic x-ray field of energy $\bar{E}$:

$$\Lambda_{ni} = \frac{2\pi}{\hbar}|\langle\Phi_n|\hat{H}_\mathrm{int}|\Phi_\mathrm{i}\rangle|^2\delta(E_{ni} - \bar{E}). \tag{7}$$

The energy difference of the states is given by E_{ni}. The interaction Hamiltonian can be expressed in terms of the nuclear current operator $\hat{\boldsymbol{j}}$ and the transverse vector potential of the x-ray field $\boldsymbol{A}$:

$$\hat{H}_\mathrm{int} = \int \hat{\boldsymbol{j}}(\boldsymbol{x}) \cdot \boldsymbol{A}(\boldsymbol{x})\,\mathrm{d}^3x. \tag{8}$$

The vector potential of the monochromatic x-ray field is just a plane wave with wavevector $\boldsymbol{k}$ and $k = E/(\hbar c)$, which gives $\boldsymbol{A}(\boldsymbol{x}) = \boldsymbol{a}\exp(\mathrm{i}\boldsymbol{k}\cdot\boldsymbol{x})$. We are concerned with the effect of vibration of the nucleus and thus distinguish internal nuclear coordinates $\boldsymbol{y}$ and the position of the centre of mass $\boldsymbol{r}$ such that $\boldsymbol{x} = \boldsymbol{r} + \boldsymbol{y}$. Equation (8) is then written as

$$\hat{H}_\mathrm{int} = \mathrm{e}^{\mathrm{i}\boldsymbol{k}\cdot\hat{\boldsymbol{r}}}\boldsymbol{a}\cdot\hat{\boldsymbol{J}}(-\boldsymbol{k}), \tag{9}$$

where $\hat{\boldsymbol{J}}$ is the spatial Fourier transform of the nuclear current operator *in the cms frame*. With this trick we accomplished a factorization of the Hamiltonian in operators of vibrations (first factor) and operators of the nucleus (last factor), and we can write

$$\langle\Phi_n|\hat{H}_\mathrm{int}|\Phi_\mathrm{i}\rangle = \langle\chi_n|\mathrm{e}^{\mathrm{i}\boldsymbol{k}\cdot\hat{\boldsymbol{r}}}|\chi_\mathrm{i}\rangle\langle\phi_n|\boldsymbol{a}\cdot\hat{\boldsymbol{J}}(-\boldsymbol{k})|\phi_\mathrm{i}\rangle. \tag{10}$$

Before we assemble this expression into (7) we revisit rule (5) to remind us that energy splittings between sublevels of nuclear ground and excited state are negligible. This allows us to write $E_{ni} - \bar{E} = \epsilon_{ni} - E$, where the ϵ_{ni} are energy differences between vibrational states only and $E = \bar{E} - E_0$ is the energy of the incident x-rays relative to the nuclear transition energy. Furthermore we want to sum over all intermediate states and average over all initial states that may be present, e.g., in a thermal distribution. After normalization to the incident photon flux, we obtain the energy-dependent absorption cross section

$$\sigma(E) = \left\langle\sum_n |\langle\chi_n|\mathrm{e}^{\mathrm{i}\boldsymbol{k}\cdot\hat{\boldsymbol{r}}}|\chi_\mathrm{i}\rangle|^2\delta(\epsilon_{ni} - E)\right\rangle\frac{2\pi}{\hbar|\boldsymbol{a}|^2}\left\langle\sum_n |\langle\phi_n|\boldsymbol{a}\cdot\hat{\boldsymbol{J}}(-\boldsymbol{k})|\phi_\mathrm{i}\rangle|^2\right\rangle. \tag{11}$$

The first term is just the excitation probability density $S(E)$ mentioned earlier, and we see immediately that $\int S(E)\,\mathrm{d}E = 1$. The excitation probability density is closely related to the self-correlation function of atomic motion $G_\mathrm{S}(\boldsymbol{x}, t)$ that was introduced by van Hove [76]:

$$S(E, \boldsymbol{k}) = \int \frac{\mathrm{d}t}{2\pi\hbar}\, \mathrm{e}^{\mathrm{i}Et/\hbar} \langle \mathrm{e}^{\mathrm{i}\boldsymbol{k}\cdot\hat{\boldsymbol{r}}(t)} \mathrm{e}^{-\mathrm{i}\boldsymbol{k}\cdot\hat{\boldsymbol{r}}(0)} \rangle$$
$$= \int \frac{\mathrm{d}x^3\,\mathrm{d}t}{2\pi\hbar}\, \mathrm{e}^{\mathrm{i}(\boldsymbol{k}\cdot\boldsymbol{x} - Et/\hbar)} G_\mathrm{S}(\boldsymbol{x}, t). \tag{12}$$

If we integrate (11) over all energies while keeping $\boldsymbol{a}$ constant we obtain $\pi/2\sigma_\mathrm{N}\Gamma$ [36], where the nuclear resonant cross section was introduced by (2) and Γ is the nuclear level width. We arrive at the simple expression

$$\sigma(E) = \frac{\pi}{2}\sigma_\mathrm{N}\Gamma S(E). \tag{13}$$

We will now proceed with estimates of $\sigma(E)$ to judge the feasibility of observation of incoherent inelastic NRS. For solid materials, $S(E)$ shows a sharp peak with width Γ around the nuclear transition energy E_0, i.e., around $E = 0$. The existence of this peak is tantamount to proof of recoilless absorption of x-rays by the nucleus, the well known Mössbauer effect [77]. Therefore we have $\Gamma S(0) = f$, the Lamb–Mössbauer factor or probability for recoilless absorption. The value of f varies between 0.05 and 0.9 for solids at room temperature [78] but vanishes for liquids and gases. The estimate for absorption 'on resonance' is then

$$\sigma(0) \approx \frac{\pi}{2}\sigma_\mathrm{N} f. \tag{14}$$

With the exception of the elastic peak, we expect $S(E)$ to be a smooth function in energy extending over an energy range that may be estimated by the Debye energy Θ. Using the normalization of $S(E)$, we can estimate for the 'off-resonance' region $\Theta S(E) \approx 1 - f$ giving

$$\sigma(E \neq 0) \approx \frac{\pi}{2}\sigma_\mathrm{N}(1 - f)\frac{\Gamma}{\Theta}. \tag{15}$$

A quantitative estimate for ^{57}Fe in metallic form gives in units of the photoelectric cross section

$$\sigma(0) \approx 560\sigma_\mathrm{pe}, \qquad \sigma(E \neq 0) \approx 0.0002\sigma_\mathrm{pe}. \tag{16}$$

The change of cross section by six orders of magnitude when moving away from the transition energy is dramatic and has serious repercussions for the normalization of measured spectra and recovery of $S(E)$. This aspect will be discussed in the next section. First, we point out the smallness of NRIXS in comparison to electronic absorption or scattering and pose the question of how such a small cross section can be observable at all.

If we can measure the probability of exciting a nucleus, we can derive $S(E)$, which contains all the phonon energies. Let us imagine a ^{57}Fe nucleus that was excited by some process. The nucleus will decay into the ground state either by emission of an x-ray photon of approximately 14.4125 keV or by transferring the excitation energy to the electron shell. In the latter case, an electron is expelled (most probably from the K shell), and the hole is quickly filled by other electrons with the emission of fluorescence x-rays. *All these decay products are emitted with some delay relative to the time of excitation of the nucleus*, and the average delay time is given by the natural lifetime of 141 ns. Figure 3 illustrates the time evolution of the scattered intensity of a material containing resonant nuclei after excitation with a SR pulse. Scattering of x-rays from electronic charge is very fast ($<10^{-12}$ s). If the energy of the incident x-rays is close to the nuclear transition energy, nuclei are excited, and delayed emission of x-rays can be observed. If only the delayed photons are counted while tuning the energy of the incident x-ray pulses, we expect to measure an event rate that is proportional to $S(E)$. An example

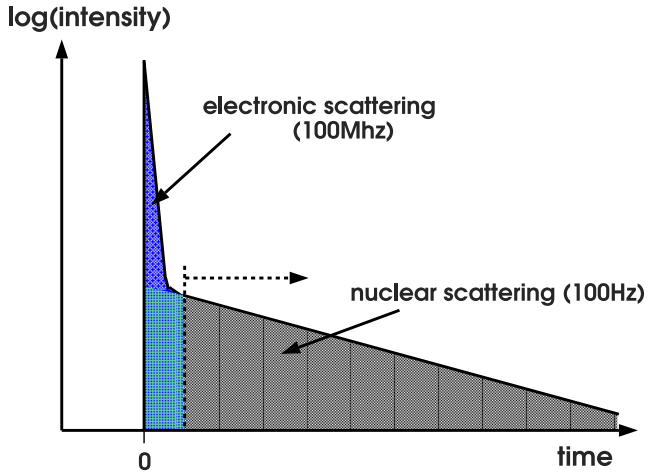

Figure 3. Scattered intensity versus time after excitation. At time zero, a SR pulse excites a material containing a nuclear resonant isotope. The scattering from electrons is prompt, i.e., almost immediately after the pulse arrived. The response of the resonant nuclei is delayed. Time discrimination permits one to distinguish nuclear and electronic scattering.

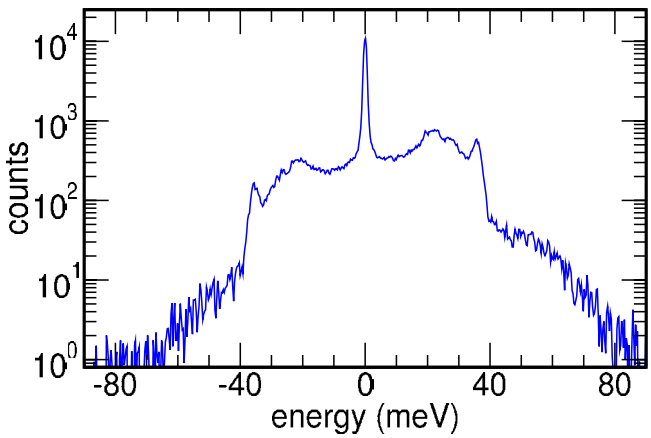

Figure 4. NRIXS spectrum of an iron foil at ambient conditions. The graph shows measured events for delayed x-ray photons versus the energy of the incident SR. Energy zero corresponds to the nuclear transition energy of 14.4125 keV. Positive energies indicate the region of phonon creation; i.e., the energy of the x-ray is too large to excite the nuclear resonance directly, and phonons must be created simultaneously. In the region of negative energies, the x-ray energy is too small, and phonons must be annihilated to produce resonant excitation.

of data collected from a metallic foil of ^{57}Fe is shown in figure 4. The time-discrimination trick removes all non-nuclear scattering of the x-rays very effectively. Thus $S(E)$ is obtained from the measured data by proper normalization, and the partial PDOS can be extracted by a mathematical procedure. Both steps will be explained in the following sections. The word 'partial' refers to the selection that has taken place by observing only vibrations at the positions of the resonant isotope.

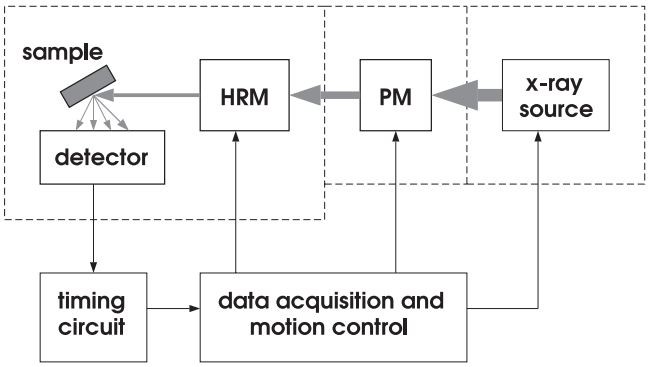

Figure 5. The set-up of a NRIXS experiment. Grey lines indicate x-rays. Solid lines symbolize flow of data or control information. The positions of PM and HRM are shown. The dashed lines indicate lead enclosures for protection of experimenters from exposure to the x-rays. The components are described in the text.

4.3. Experimental procedure

A schematic diagram of the typical experimental set-up that can be found at third-generation SR facilities is shown in figure 5. The x-ray source consists of electrons that are orbiting in the storage ring and periodically pass through an undulator. The x-rays are monochromatized in two steps using a premonochromator (PM) and a high-resolution monochromator (HRM) to an energy bandwidth that is narrower than the phonon spectrum of the samples. The HRM is tuned around the nuclear transition energy, and the x-rays excite the nuclei in the sample. The re-emitted radiation is observed with the APD detector. The timing circuit measures the time elapsed between excitation and re-emission and removes prompt events. Numbers given in this subsection are typical for the NRS beamline 3-ID at the Advanced Photon Source. More information on SR facilities with emphasis on NRS methods can be found in [79].

X-ray source. SR is created by charged particles that are stored in closed orbits. To keep the particles in closed orbits they have to be accelerated perpendicular to their propagation direction. Electrons with an energy of 7 GeV are kept on an approximately circular orbit with a circumference of about 1.1 km. The electrons are highly relativistic, and they need 3.68 μs for one revolution. The x-rays produced by the bending magnets that keep the electrons orbiting are moderately intense. X-rays of sufficient brightness for NRS experiments are obtained from undulators, which are devices with a spatially periodic magnetic field. The electrons propagate through the field and experience small periodic deviations from a straight line. The accelerations exerted by the periodic field lead to the emission of very collimated and intense x-rays.

The electrons in the storage ring may occupy a finite number of stable positions within an orbit called buckets, e.g., 1296 buckets separated by 0.85 m or 2.84 ns. Buckets that are filled with electrons are called bunches, and the actual pattern of bunches produces the time structure of the SR. The standard time structure at the Advanced Photon Source consists of 23 bunches with a separation of 153 ns. It is very important for NRS experiments that the time between bunches is larger than the dead time of the detector (20 ns) and at least comparable to the nuclear lifetime in order to obtain appreciable signal rates.

A typical size of a bunch is 0.036 mm vertical, 0.56 mm horizontal, and 20 mm along the direction of propagation. The transverse size of the bunch determines the transverse size of the x-ray source. Each bunch produces an x-ray pulse of 70 ps duration when passing through

the undulator. Another important parameter is the divergence or angular width of the radiation produced, which is typically 9 μrad vertical and 34 μrad horizontal. For a sample that is mounted 35 m from the undulator, the beam size becomes 0.35×1.75 mm^2.

Monochromators. The undulator creates a broad energy band of x-rays (the so-called 'white beam') that ranges from about 6 keV up to several 100 keV, even though there are distinct peaks with enhanced intensity and widths of about 200 eV. The PM filters an energy band of about 1 eV from the white beam. This bandwidth is not narrow enough for performing phonon spectroscopy, but the total power in the x-ray beam is reduced from 1000 to 0.1 W. The reduction in power is important because of the temperature sensitivity of the HRM. Two diamond crystals in non-dispersive arrangement operate at (111) Bragg reflections to perform the task of filtering and power reduction. In the experiment, the PM is adjusted to transmit around the nuclear resonance energy, and the undulator is tuned to produce an intense peak at this energy.

The high-resolution monochromator reduces the energy bandwidth of the x-rays to approximately 1 meV, and its tunability range easily covers the 200 meV energy range where the probability for phonon excitation or annihilation is high. The principle of high-resolution monochromatization in this region of the electromagnetic spectrum relies upon the use of Bragg diffraction from a series of perfect single crystals. The diffraction planes and their orientation with respect to the crystal surfaces are chosen to achieve optimal performance in terms of efficiency and energy resolution and are selected when the monochromator is fabricated. A review of high-resolution monochromators for NRS spectroscopy has recently been given in [65]. In order to take high-quality spectroscopic data, the energy response of the instrument must be known. In the case of NRIXS, the energy response is determined solely by the HRM. The energy resolution function of the monochromator is measured using coherent elastic NRS and used to subtract the elastic scattering contributions from the NRIXS spectra.

Detector and timing circuit. The nuclear resonant signal is discriminated from the much more abundant non-resonant signal by using a time-filtering technique (see figure 3). For this we need a detector with a very good time resolution and an excellent dynamic range is required; i.e., after the intense pulse of prompt, non-resonant photons, the detector has to quieten down in a reasonably short time. The best x-ray detectors with such qualities are APDs and their NRS applications have been reviewed in [64]. The typical time resolution of a detector using a 10×10 mm^2 area silicon APD is about 1 ns.

Additional electronic components are needed to apply the time-filtering technique. First we need to know when the x-ray pulses arrive at the sample. The x-ray pulses will be synchronized with the bunch pattern, which can be produced electronically from the operation parameters of the storage ring. These signals, the 'bunch clock', will be compared to the output signal of the APD detector, and anticoincidence logic filters out the delayed events. Besides the delayed events that originate in NRS, electronic noise may fake 'delayed events' because such pulses are asynchronous with the bunch pattern. Electronic noise created by the detector is unavoidable but typically small (see figure 6). The noise-event rate is independent of the incident x-ray energy and is measured by tuning the monochromator sufficiently far away from the resonance.

4.4. Interpretation

In this section, we will explain the normalization procedure for NRIXS spectra and the extraction of the vibrational DOS. We will also discuss several other quantities that can be calculated from the spectra and their physical meaning.

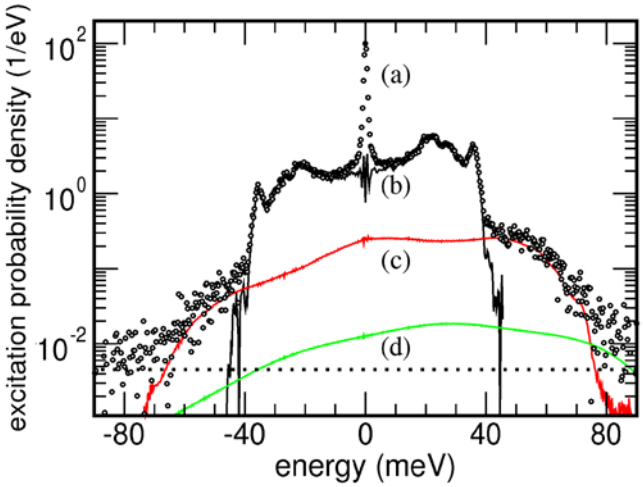

Figure 6. Decomposition of the normalized NRIXS spectrum of figure 4. The graph shows the data normalized using (20) including the elastic peak (a), the one-phonon term $S_1(E)$ (b), the two-phonon term $S_2(E)$ (c), and the sum of the higher-order terms (d). The decomposition procedure is explained in the text. The dotted line indicates the noise level in the experiment.

Normalization. From the estimate (16), it follows that, near the elastic peak of the NRIXS spectrum, the penetration depth of the x-rays in the sample is dominated by the nuclear resonant absorption cross section. Away from the elastic peak, electronic absorption determines the penetration depth. This situation leads to a suppression of the elastic peak in the measured data because the number of scattering nuclei is reduced by the smaller penetration depth, and the measured event rate is given by

$$I(E) = A\{S(E) - C\delta(E)\}. \tag{17}$$

We need to determine the normalization constant A, but the suppression effect also produces the second term with an unknown, sample-dependent number C. This problem is circumvented by use of the first moment of $S(E)$ for normalization [33]. We use (12) to write

$$\begin{aligned}\int ES(E)\,\mathrm{d}E &= \mathrm{i}\hbar\left(\frac{\mathrm{d}}{\mathrm{d}t}\langle \mathrm{e}^{\mathrm{i}\boldsymbol{k}\cdot\hat{\boldsymbol{r}}(t)}\mathrm{e}^{-\mathrm{i}\boldsymbol{k}\cdot\hat{\boldsymbol{r}}(0)}\rangle\right)_{t=0} \\ &= \langle[\mathrm{e}^{\mathrm{i}\boldsymbol{k}\cdot\hat{\boldsymbol{r}}}, \hat{H}]\mathrm{e}^{-\mathrm{i}\boldsymbol{k}\cdot\hat{\boldsymbol{r}}}\rangle,\end{aligned} \tag{18}$$

where $\hat{H}$ is the Hamiltonian of the vibrational degrees of freedom. For the calculation of the commutator, only the kinetic energy term $\hat{\boldsymbol{p}}^2/(2M)$ needs to be retained, and with $[\hat{r}_\mathrm{i}, \hat{p}_j] = \mathrm{i}\hbar\delta_{ij}$ and $\langle\hat{\boldsymbol{r}}\rangle = 0$, we obtain Lipkin's result [80] that the first moment only depends on properties of the nuclear isotope:

$$\int ES(E)\,\mathrm{d}E = \frac{\hbar^2\boldsymbol{k}^2}{2M} = E_\mathrm{R}, \tag{19}$$

where M is the mass of the nuclear isotope, and E_R is the recoil energy defined in (6). Application of this rule to the normalization problem results in the expression

$$\int EI(E)\,\mathrm{d}E = AE_\mathrm{R}, \tag{20}$$

which permits us to calculate the normalization constant A. The integration of (17) also provides

$$C = 1 - \frac{1}{A}\int I(E)\,\mathrm{d}E. \tag{21}$$

For the data of figure 4, we obtain $C = 0.69$, indicating the importance of using the first-moment normalization.

Moments. Several higher-order moments were calculated by Lipkin [81], and we will briefly present the results. The centred moments of the excitation probability are defined by

$$\begin{aligned} M_n &= \int (E - E_\mathrm{R})^n S(E)\,\mathrm{d}E \\ &= (\mathrm{i}\hbar)^n \left(\frac{\mathrm{d}^n}{\mathrm{d}t^n} \mathrm{e}^{\mathrm{i}E_\mathrm{R}t/\hbar} \langle \mathrm{e}^{\mathrm{i}\boldsymbol{k}\cdot\hat{\boldsymbol{r}}(t)} \mathrm{e}^{-\mathrm{i}\boldsymbol{k}\cdot\hat{\boldsymbol{r}}(0)} \rangle \right)_{t=0}. \end{aligned} \tag{22}$$

By definition $M_0 = 1$, and the centred first moment as discussed above vanishes, $M_1 = 0$. The latter result was obtained under the reasonable assumption that the binding potential only depends on the atomic positions and not on their momenta.

Some of the higher-order moments assume a useful physical meaning. A calculation of the second-order moment results in

$$M_2 = 4E_\mathrm{R}\left\langle \frac{(\boldsymbol{s}\cdot\hat{\boldsymbol{p}})^2}{2M} \right\rangle = 4E_\mathrm{R}E_\mathrm{kin}(\boldsymbol{s}), \tag{23}$$

where $\boldsymbol{s} = \boldsymbol{k}/k$ gives the direction of the incident photon. The bracketed term represents the contribution to the average kinetic energy of the resonant atom from its momentum along $\boldsymbol{s}$. The derivation required that $\langle\hat{\boldsymbol{p}}\rangle = 0$, which is generally the case in bound systems. In the classical limit of large temperatures, we expect $E_\mathrm{kin}(\boldsymbol{s}) \to k_\mathrm{B}T/2$ and M_2 to increase linearly with temperature. For finite temperatures, the zero-point motion of the bound atoms will increase the average kinetic energy and therefore $M_2 > 2E_\mathrm{R}k_\mathrm{B}T$. The data that are displayed in figure 4 were measured at $T = 300$ K and give $E_\mathrm{kin}(\boldsymbol{s}) = 14.16(8)$ meV or 165(1) K demonstrating the quantum effect of zero-point motion.

The third-order moment gives a measure of the binding strength of the atom in the lattice. Using (22) one obtains

$$M_3 = 2\hbar^2c^2\frac{E_\mathrm{R}^2}{E_0^2}\langle(\boldsymbol{s}\cdot\boldsymbol{\nabla})^2V\rangle = 2\hbar^2c^2\frac{E_\mathrm{R}^2}{E_0^2}D(\boldsymbol{s}), \tag{24}$$

where the bracketed term has the character of a second-order spatial derivative of the atomic potential V and can be associated with a mean force constant that holds the atom in its position. If the atoms in the lattice are bound by harmonic potentials, V is quadratic in the atomic displacements, and the second derivative should be constant, i.e., independent of temperature. The temperature variation of D in real materials can serve as a measure for anharmonicity of the lattice vibrations. The data that are displayed in figure 4 provide us with $D = 180(4)$ N m^{-1}. It is important to note that no vibrational model was necessary to obtain the relationships for the moments.

Phonon density of states. The interpretation of NRIXS spectra can go far beyond the calculation of a few moments if we make assumptions about the interatomic potential V. The most widespread and usually quite good approximation that V is quadratic in the atomic

displacements leads to the harmonic lattice, and the equation of motion can be integrated. The excitation probability can then be rewritten in a physically meaningful way as

$$\begin{aligned} S(\boldsymbol{s}, E) &= f(\boldsymbol{s})\delta(E) + \sum_{n=1} S_n(\boldsymbol{s}, E), \\ S_1(\boldsymbol{s}, E) &= \frac{E_\mathrm{R}}{E(1-\exp(-\beta E))} g(\boldsymbol{s}, |E|), \\ S_n(\boldsymbol{s}, E) &= \frac{1}{nf} \int S_{n-1}(\boldsymbol{s}, E') S_1(\boldsymbol{s}, E - E')\, \mathrm{d}E', \qquad n > 1, \end{aligned} \tag{25}$$

where the individual terms S_n correspond to n-phonon contributions. The delta-distribution term describes elastic scattering. The probability for this process is given by the Lamb–Mössbauer factor f. The probability $\mathrm{d}P_1$ of creating ($E > 0$) or annihilating ($E < 0$) one phonon of energy $|E|$ is given by the first-order term, i.e., $\mathrm{d}P_1 = S_1(E)\,\mathrm{d}E$. The second-order term incorporates the participation of two phonons with energies that add to E. Integration of the individual terms in (25) yields probabilities

$$P_n = \int S_n(E)\,\mathrm{d}E = f\frac{(-\ln f)^n}{n!} \tag{26}$$

that resemble a Poissonian distribution. We immediately obtain $\langle n\rangle = -\ln f$ and may conclude that small values of f will increase the importance of higher-order phonon terms. The data in figure 4 provide $P_0 = f = 0.796(2)$ and thus $\langle n\rangle = 0.23$, $P_1 = 0.18$, and $P_2 = 0.02$. In materials with reasonably large values of f, i.e., strong elastic scattering, the one-phonon term will usually dominate. We will return to this topic in a moment.

For a given inverse temperature β, all terms in (25) are generated from the projected partial PDOS $g(\boldsymbol{s}, E)$. Here 'projected' refers to the dependence on the direction of the incident x-rays and 'partial' emphasizes the fact that only the vibrations of the resonant atoms are probed. The general properties of $g(\boldsymbol{s}, E)$ with consideration of the crystal symmetry have been discussed in [36]. For example, in crystals with cubic symmetry, $g(\boldsymbol{s}, E)$ is isotropic, i.e., independent on the direction of the incident x-rays. We can calculate $g(\boldsymbol{s}, E)$ from $S(\boldsymbol{s}, E)$ by inversion of the multiple convolutions using the 'Fourier–log method' [82]. The application of this method to NRIXS spectra has been described before [35, 83–85]. We now outline the ideas of the Fourier–log method.

If we apply a Fourier transformation to (25), the convolutions turn into products giving

$$\frac{\tilde{S}_n}{f} = \frac{1}{n!}\left(\frac{\tilde{S}_1}{f}\right)^n. \tag{27}$$

We use this expression to perform the summation, which now leads to a closed form:

$$\tilde{S} = f + \sum_{n=1} \tilde{S}_n = f\exp\left(\frac{\tilde{S}_1}{f}\right). \tag{28}$$

This expression is easily inverted to give the Fourier-transformed one-phonon contribution. Finally we obtain

$$S_1 = \mathcal{F}^{-1}\left[f\ln\left(\frac{\tilde{S}}{f}\right)\right]. \tag{29}$$

Some numerical aspects of this procedure have been discussed in [84]. In particular, removing the elastic peak in the NRIXS spectrum prior to Fourier transformation is advantageous. Results of the decomposition procedure applied to the data from figure 4 are shown in figure 6. As expected from our estimates, the one-phonon term dominates. Beyond the visible energy cut-off, we clearly see the two-phonon contribution to the spectrum, and higher-order terms

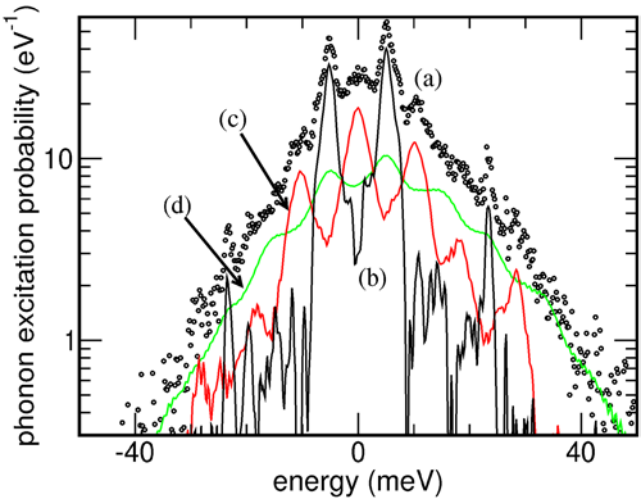

Figure 7. Decomposition of the normalized NRIXS spectrum of a thin film of α-Sn. The graph shows the data normalized using (20) and the elastic peak removed (a), the one-phonon term $S_1(E)$ (b), the two-phonon term $S_2(E)$ (c), and the sum of the higher-order terms (d). The decomposition procedure is explained in the text. The data were taken from [56].

give a contribution above 70 meV but are otherwise mostly negligible. This situation changes substantially for lower values of f as demonstrated in figure 7. In this case of a thin film of α-Sn [56], we have $f = 0.14(2)$ and thus $\langle n \rangle = 1.97$, $P_1 = 0.28$, $P_2 = 0.27$, and $P_3 = 0.18$. The one-phonon contribution is clearly not the dominating term. The sharp features in S_1, e.g., the optical phonon mode around 23 meV, appear much weaker in the actual spectrum because of the rather smooth contributions from the higher-order terms.

The one-phonon term S_1 is proportional to the projected partial PDOS, and we obtain from (25)

$$g(\boldsymbol{s}, E) = \begin{cases} \dfrac{E}{E_\mathrm{R}} \tanh \dfrac{\beta E}{2} (S_1(\boldsymbol{s}, E) + S_1(\boldsymbol{s}, -E)) & \text{for } E > 0, \\ 0 & \text{for } E \leqslant 0. \end{cases} \tag{30}$$

The projected partial PDOS is normalized by $\int g(\boldsymbol{s}, E)\, \mathrm{d}E = 1$ and describes how one degree of translational freedom of the resonant atom is distributed over the collective vibrational modes of the lattice. From (12) it follows that the scattering cross section is sensitive to motions of the atom along the direction of the incident x-ray photon only. If one samples three independent directions of space by changing the photon direction relative to the material, all three degrees of freedom are covered. The sum of those three projected partial PDOS provides the partial PDOS. For crystals with cubic symmetry, the PDOS is simply $3g$ with an isotropic g [36]. In figure 8, we show the PDOS of iron metal, which is cubic (bcc) at ambient conditions. In the same graph, the relationship between the one-phonon term S_1 and the PDOS is displayed. The scaling factor amplifies higher energies of S_1 and their errors. The accuracy of the extracted PDOS is therefore reduced for higher energies. For cases with lower values of f, the errors in the reconstructed S_1 may increase to a level that renders the PDOS extraction impracticable [86].

In the above examples, iron metal and α-tin, the crystal structure is cubic, and all atoms in the lattice are resonant. Therefore the quantity determined via (30) is the total PDOS and may be used to calculate thermodynamic quantities pertinent to lattice vibrations. The partition

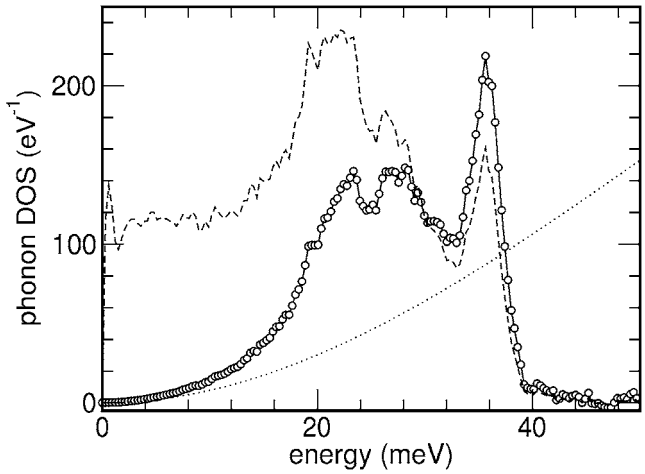

Figure 8. The PDOS of iron metal (bcc). The solid curve shows $3g$ calculated from the one-phonon contribution to the excitation probability density using (30). The dashed curve shows $S_1(E) + S_1(-E)$. The energy-dependent factor of (30) emphasizes the higher energies and is represented by the dotted curve.

function for the harmonic lattice is given by

$$\ln Z^N = -3N \int \ln\left(2 \sinh \frac{\beta E}{2}\right) g(E)\, \mathrm{d}E, \tag{31}$$

where N is the number of atoms. We obtain for the vibrational energy per atom

$$U = -\frac{\partial \ln Z}{\partial \beta} = \frac{3}{2} \int E \coth \frac{\beta E}{2} g(E)\, \mathrm{d}E. \tag{32}$$

Here the zero-point motion produces the contribution $U(\beta \to \infty) = (3/2) \int Eg(E)\, \mathrm{d}E$. The vibrational entropy per atom S and the free energy per atom F also follow from the partition function:

$$S = k_\mathrm{B} \beta U + k_\mathrm{B} \ln Z, \qquad F = -\frac{1}{\beta} \ln Z. \tag{33}$$

Finally, we give an expression for the specific heat per atom at constant volume:

$$c_V = \frac{\partial U}{\partial T} = k_\mathrm{B} \beta^2 \frac{\partial^2 \ln Z}{\partial \beta^2} = 3k_\mathrm{B} \int \left(\frac{\beta E}{2 \sinh(\beta E/2)}\right)^2 g(E)\, \mathrm{d}E \tag{34}$$

with the expected high-temperature limit of $c_V(\beta \to 0) = 3k_\mathrm{B}$.

In most applications, the resonant atoms are only one of several constituents of the material under investigation, and the quantities given in (31)–(34) give only the contribution of the resonant atoms. This may not be representative for the thermodynamic behaviour of the material, and the experimentally obtained data have to be complemented by calculations. Nevertheless vibrational entropies from the PDOS have been used successfully to explain order–disorder effects in iron alloys [62, 63].

4.5. Sound velocities

In general, the PDOS of a particular atom species does not give information about the PDOS of another atom species in the material or the total PDOS—with one important exception.

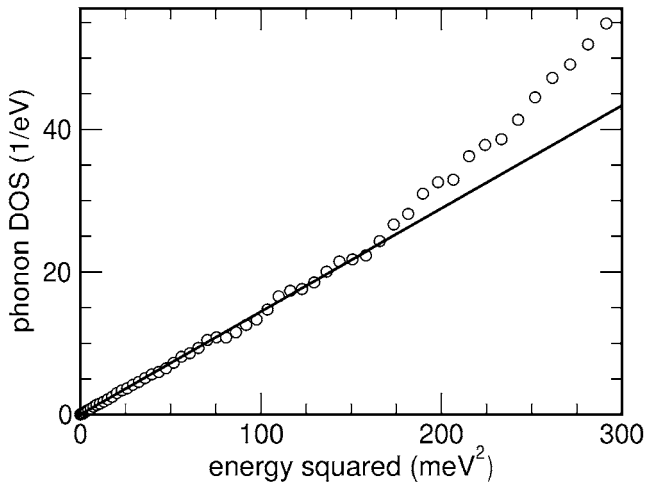

Figure 9. The low-energy region of the PDOS of iron metal. The straight line represents a parabolic fit for energies less than 13 meV. At higher energies, the PDOS starts to deviate from (35). The slope of the straight line allows one to calculate the Debye sound velocity according to (35).

Solids show Debye-like behaviour of the PDOS at small energies, and the individual PDOS are related by a simple scaling law [87]. For small energies, we can write

$$g(\boldsymbol{s}, E) = \frac{M}{\rho} \frac{E^2}{2\pi^2 \hbar^3 v_{\mathrm{s}}^3}, \tag{35}$$

where M is the mass of the resonant nucleus, and ρ is the mass density of the solid. The projected sound velocity v_{s} is defined as an average over the directionally and mode-dependent sound velocities by

$$\frac{1}{v_{\mathrm{s}}^3} = \sum_{m=1}^{3} \int \frac{\mathrm{d}\Omega_q}{4\pi} \frac{(\boldsymbol{s} \cdot \boldsymbol{p}_{qm})^2}{c_{qm}^3}, \tag{36}$$

where $\boldsymbol{p}_{qm}$ and c_{qm} are the polarization vector and velocity, respectively, of an acoustic phonon of type m propagating in the direction $\boldsymbol{q}$. For cubic crystals, the directional dependence of g and thus of v_{s} disappears. Randomly oriented crystallites, isotropic materials, and aggregates are well described by averaging over the direction s. In these cases without directional dependence, the average of v_{s} is equivalent to the Debye sound velocity defined by

$$\frac{1}{v_{\mathrm{D}}^3} = \frac{1}{3} \sum_{m=1}^{3} \int \frac{\mathrm{d}\Omega_q}{4\pi} \frac{1}{c_{qm}^3}. \tag{37}$$

In practice, the Debye sound velocity is obtained from a material with known density by adjusting a parabola to the low-energy region of the PDOS that was extracted from the NRIXS data according to (35). In figure 9, we demonstrate this procedure for the low-energy region of the PDOS of iron metal from figure 8. One obtains $v_{\mathrm{D}} = 3.49(5)$ km s^{-1} from the slope of the straight line and the known density of iron metal. The importance of using NRIXS to determine sound velocities instead of ultrasonic methods or Brillouin scattering lies in its applicability to very small samples under extreme pressure conditions; see e.g. [38]. In particular, the sound velocities of iron-containing minerals and alloys are of great interest in geophysical research.

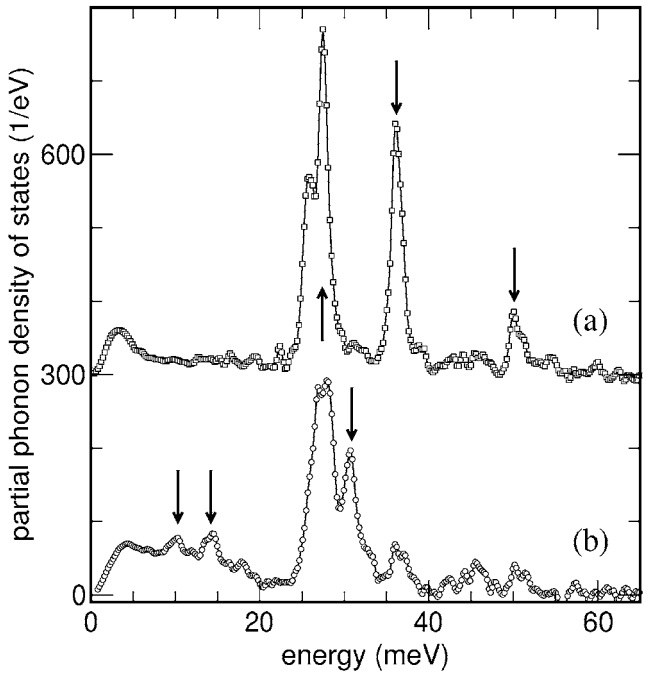

Figure 10. The ^{57}Fe PDOS of a single crystal of Fe(TPP)(2-MeImH), a deoxyheme protein model compound. The direction of the incident x-rays was either parallel (a) or perpendicular (b) to the molecular plane. Several vibrational modes indicated by arrows show a pronounced polarization. The data are taken from [45].

4.6. Phonon polarization

The dependence of the measured vibrational excitation probability on the direction of the incident x-rays permits us to determine the polarization of vibrational modes. Imagine a vibrational mode that causes an atomic displacement given by

$$\boldsymbol{r}(t) = \boldsymbol{p}\alpha(t), \tag{38}$$

where $\boldsymbol{p}$ describes the phonon polarization. If the direction of the incident x-rays is perpendicular to the displacement, i.e., $\boldsymbol{p} \cdot \boldsymbol{k} = 0$, then (12) implies that the corresponding vibrational mode cannot be excited. This directional dependence has been observed in single-crystalline iron borate, $FeBO_3$ [35], and in single crystals of organic molecules [42, 45]. In figure 10, we show the PDOS of a single crystal of Fe(TPP)(2-MeImH). The study of the ^{57}Fe PDOS of deoxyheme protein model compounds is expected to give direct insight into the role of iron dynamics in important biological reactions of heme proteins [43–45]. The resonant iron atoms are located in the centre of the planar Fe(TPP)(2-MeImH) molecules, the orientation of which is maintained in the crystal structure. In the experiment, the molecular planes in the crystal were aligned either parallel or perpendicular to the x-ray beam. Vibrational modes at 10, 14, 31 meV clearly have out-of-plane polarizations, whereas modes at 27, 36, and 50 meV show mostly in-plane character. A detailed analysis and assignment of the vibrational modes of this model compound was presented in [45].

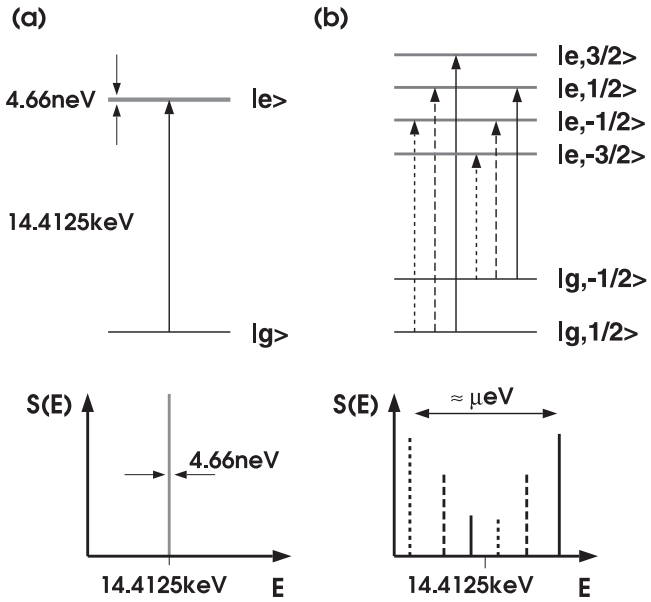

Figure 11. The influence of the electronic environment on the nuclear level scheme. Panel (a) shows the energy levels of a bare ^{57}Fe nucleus. The nuclear transition $|g\rangle \rightarrow |e\rangle$ causes a sharp resonance in the excitation probability density $S(E)$. However, the spin quantum numbers of the ground and excited states are $1/2$ and $3/2$, respectively, leading to a twofold and fourfold degeneracy of nuclear levels. If the nucleus is embedded in its natural environment the degeneracy may be lifted as shown in panel (b) for a magnetic dipole interaction. $S(E)$ now features several nuclear transitions. The energy separation of the outer lines is about 15.5 neV T^{-1}, which is potentially much larger than the nuclear level width.

5. SMS

Here we explain the ideas behind SMS. The index-of-refraction model serves to calculate the propagation of x-rays in materials containing resonant nuclei. Using this model, we discuss salient features of time spectra that are relevant to the extraction of hyperfine interaction parameters. Also the experimental requirements are briefly discussed.

5.1. Principles

In solids the probability that NRS from low-energy resonances occurs without change in the vibrational state is appreciable. This quantity was introduced in the previous section as the Lamb–Mössbauer factor, $f = \Gamma S(0)$, in terms of the phonon excitation probability density of (12). The corresponding transitions are indicated in panel (b) of figure 2 as solid lines. A more detailed view is presented in figure 11. Now that vibrational transitions are excluded the splitting of the nuclear levels becomes visible and measurable. The nuclear level splitting is caused by interaction of the nucleus with the electronic environment and is known as hyperfine interaction. In our example in figure 11, the ground and excited states of the ^{57}Fe nucleus have spin quantum numbers of $1/2$ and $3/2$, respectively. In the case of the isolated nucleus, the energy levels show twofold and fourfold degeneracy. Here the rotational symmetry of the vacuum state is not broken. We now break this symmetry, which is equivalent to the introduction of interactions.

A case of importance is axial symmetry and is usually observed in the form of an axially symmetric electric field gradient at the nucleus. The field gradient is created by the electronic

environment and couples to the quadrupole moment of the nucleus. The axial symmetry removes the degeneracy only partially because we still maintain mirror symmetry along the axis. The energy splitting for $I > 1/2$ is given by

$$E_m = \Delta \frac{3m^2 - I(I+1)}{2I(2I-1)} \qquad m = -I, \ldots, I, \tag{39}$$

where Δ is called the electric quadrupole splitting. For the ^{57}Fe case, the nuclear quadrupole moment of the spin-1/2 ground state vanishes leaving it degenerate. The axial symmetry causes a split of the excited state into two twofold-degenerate levels. In particular, we obtain a characteristic two-line pattern with $E_{\pm 3/2} - E_{\pm 1/2} = \Delta$.

Panel (b) of figure 11 demonstrates the effect of a magnetic field on the nuclear levels. The presence of the magnetic field corresponds to unidirectional symmetry, which removes the degeneracy completely. The energy splitting is given by

$$E_m = -\mu B \frac{m}{I} \qquad m = -I, \ldots, I, \tag{40}$$

where μ, I are the magnetic moment and spin of the nuclear state, B is the magnetic field at the nucleus, and m is the spin-projection quantum number. For ^{57}Fe, the magnetic moments of the ground and excited state take values of $\mu_g = 2.86$ neV T^{-1} and $\mu_e = -4.89$ neV T^{-1}. As a result of the broken symmetry, one observes several nuclear transitions within an energy range of the order of microelectronvolts or less. The 14.4125 keV transition of ^{57}Fe has M1 multipolarity, and, with unidirectional symmetry, the individual transitions shown in panel (b) of figure 11 follow dipole selection rules, i.e., $|m_e - m_g| \leqslant 1$. This results in a characteristic six-line pattern.

In addition to the breaking of rotational symmetry resulting in the interactions discussed above, one expects a renormalization of the energy of nuclear levels due to the presence of s electrons in the nuclear volume. Here, no rotational symmetry breaking occurs. The observable result is a slight shift of the transition energy that is proportional to the density of the s electrons in the nuclear volume. This so-called isomer shift can only be measured by comparison of different materials; e.g., for ^{57}Fe the isomer shift is usually given relative to ^{57}Fe nuclei in iron metal at ambient conditions.

The presence of both magnetic dipole and electric quadrupole interactions is equivalent to complete rotational symmetry breaking. In this case, energy levels and selection rules have to be obtained by diagonalization of the corresponding Hamiltonian. The origin and interpretation of hyperfine interactions is encountered in the extended history of Mössbauer spectroscopy and described in great detail in a large body of literature. Recent reviews with emphasis on NRS with SR have been given in [88–91].

In an elastic coherent process, such as nuclear forward scattering, the different nuclear transitions can be excited simultaneously by a short x-ray pulse with sufficient bandwidth. The different nuclear transitions are then analogous to a set of oscillators with slightly different energies that are excited in phase. Shortly after the x-ray pulse has passed, the de-excitation begins, also in phase, but soon the increasing phase difference leads to destructive interference and then again to a constructive interference. This characteristic behaviour is illustrated in figure 12. It is the basic process that leads to oscillations in the decay of forward-scattered radiation.

5.2. Experimental procedure

A schematic diagram of the typical experimental set-up for SMS that can be found at third-generation SR facilities is shown in figure 13. The individual components are very similar to

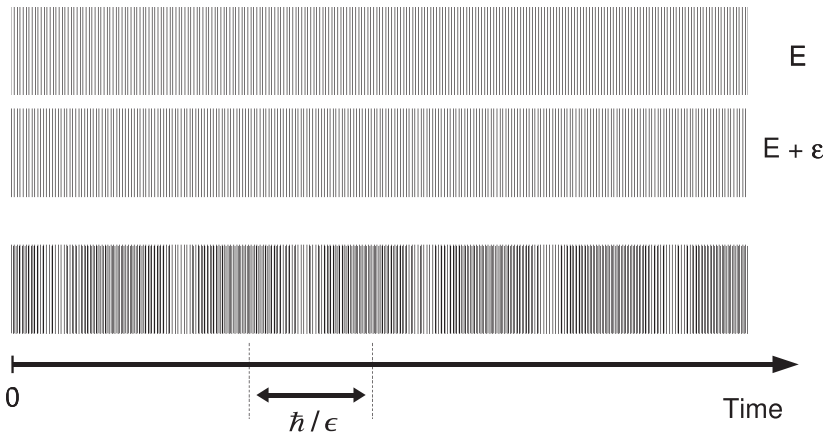

Figure 12. The coherent response of a nuclear ensemble to excitation with a SR pulse at time zero. The two upper traces symbolize the response of two nuclear transitions with slightly different energies E and $E + \epsilon$. The coherent superposition of these contributions shows a modulation with frequency $\hbar/\epsilon$ (bottom). The time oscillations reproduce the energy difference of the nuclear transitions and therefore the nuclear level splitting.

those introduced in the previous section on NRIXS (compare figure 5). The x-ray source are electrons that are orbiting in the storage ring, periodically pass through an undulator, and create short x-ray pulses of high brightness. The x-rays are monochromatized in two steps (PM and HRM) to an energy bandwidth that is as small as is practicably achievable with reasonable efficiency. The HRM is tuned to the nuclear transition energy and kept as stable as possible. X-rays that are transmitted through the sample excite the resonant nuclei coherently. The re-emitted radiation is observed with the APD detector. The timing circuit measures the time elapsed between excitation and re-emission and removes prompt events. The delayed events are mapped as a function of elapsed time—this constitutes the time spectrum of the nuclei in the sample. The distance between the sample and detector should be large enough to avoid nuclear incoherently scattered photons reaching the APD. In contrast to NRIXS, not the total intensity but rather the spectral intensity after the monochromator is important for SMS experiments. If the energy bandwidth is decreased while maintaining the spectral intensity, SMS experiments will benefit from the reduced abundance of non-resonant events. NRIXS would benefit from the improved energy resolution, alas at the expense of a reduction in measured signal. For SMS, the HRM essentially takes the role of a band-pass filter around the nuclear transition energy.

5.3. Index-of-refraction model

Extensive treatments on the theory of NRS have been given, for example, in [89, 90]. The special but very useful case of nuclear forward scattering [92] uses coherent elastic scattering into the direction of the incident radiation. Here we will use the index-of-refraction model [93] to gain a unified understanding of energy-resolved Mössbauer spectroscopy and SMS.

Transmission function. For x-ray energies, materials may be characterized by an electric susceptibility tensor $\chi(x, \omega)$ depending on the space coordinate and energy. The magnetic susceptibility is negligible. The tensor χ defines a linear relation between the electric field and the polarizability of the material. Maxwell's equations require that each energy component of

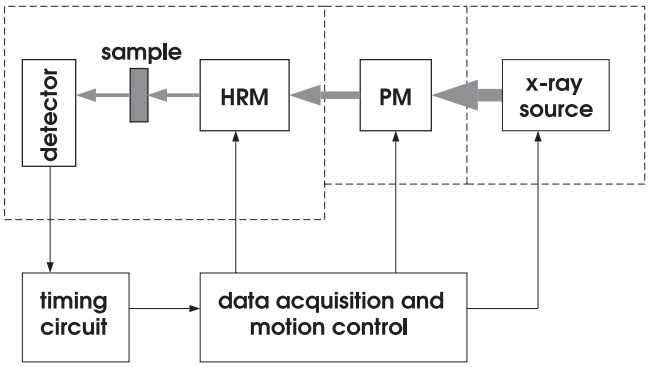

Figure 13. The set-up of a SMS experiment. Grey lines indicate x-rays. Solid lines symbolize flow of data or control information. The positions of PM and HRM are shown. The dashed lines indicate lead enclosures for protection of experimenters from exposure to the x-rays. The components are described in the text.

the electric field inside the material satisfies

$$\begin{aligned} &c^2\boldsymbol{\nabla}\times\boldsymbol{\nabla}\times\boldsymbol{E}(\boldsymbol{x},\omega)-\omega^2\boldsymbol{E}(\boldsymbol{x},\omega)=4\pi\omega^2\boldsymbol{\chi}(\boldsymbol{x},\omega)\boldsymbol{E}(\boldsymbol{x},\omega),\\ &\boldsymbol{\nabla}\cdot\boldsymbol{E}(\boldsymbol{x},\omega)=\boldsymbol{\nabla}\cdot(\boldsymbol{\chi}(\boldsymbol{x},\omega)\boldsymbol{E}(\boldsymbol{x},\omega)). \end{aligned} \tag{41}$$

The weak response of materials to x-ray fields leads to susceptibilities of the order of 10^{-5} or less, and we approximate the constraint imposed in the second equation by $\boldsymbol{\nabla}\cdot\boldsymbol{E}=0$. This implies that an x-ray field propagating through a medium remains transverse. Now let us consider solutions of (41) that are almost plane waves:

$$\boldsymbol{E}(\boldsymbol{x},\omega)=\boldsymbol{A}(\boldsymbol{x},\omega)\mathrm{e}^{\mathrm{i}\boldsymbol{k}\cdot\boldsymbol{x}}, \tag{42}$$

where $c|\boldsymbol{k}|=\omega$, and the function $\boldsymbol{A}$ shows only weak variation with position. Solutions of this type will properly describe the forward propagation of an x-ray field through matter in the absence of Bragg and Laue excitations. We substitute the electric field in (41) and use the approximate constraint to obtain

$$\begin{aligned} &2\mathrm{i}(\boldsymbol{k}\cdot\boldsymbol{\nabla})\boldsymbol{A}+\nabla^2\boldsymbol{A}=-4\pi\frac{\omega^2}{c^2}\boldsymbol{\chi}\boldsymbol{A},\\ &\boldsymbol{\nabla}\cdot\boldsymbol{A}+\mathrm{i}\boldsymbol{k}\cdot\boldsymbol{A}=0. \end{aligned} \tag{43}$$

The strongest spatial variation of the function $\boldsymbol{A}$ occurs in the direction of $\boldsymbol{k}$, and one can neglect the second derivatives. With the notation $\boldsymbol{k}=\boldsymbol{s}\omega/c$, the field amplitude satisfies the first-order differential equation

$$\frac{\mathrm{d}}{\mathrm{d}\eta}\boldsymbol{A}(\boldsymbol{y}+\eta\boldsymbol{s},\omega)=2\pi\mathrm{i}\frac{\omega}{c}\boldsymbol{\chi}(\boldsymbol{y}+\eta\boldsymbol{s},\omega)\boldsymbol{A}(\boldsymbol{y}+\eta\boldsymbol{s},\omega), \tag{44}$$

where η takes the role of an affine parameter. Now assume that small volumes with almost constant field amplitude $\boldsymbol{A}$ exist almost everywhere in the medium. Then we can volume-average (44), resulting in a formally identical equation that now contains an averaged susceptibility. If the medium is sufficiently homogeneous, the averaged susceptibility will be independent of location, and the averaged version of (44) can be integrated along a path that lies completely inside the material to give

$$\boldsymbol{A}(\boldsymbol{y}+\eta\boldsymbol{s},\omega)=\exp\left(2\pi\mathrm{i}\eta\frac{\omega}{c}\bar{\boldsymbol{\chi}}(\omega)\right)\boldsymbol{A}(\boldsymbol{y},\omega), \tag{45}$$

where $\bar{\boldsymbol{\chi}}(\omega)$ denotes the spatially averaged susceptibility tensor. This equation combined with (42) results in the compact expression

$$\begin{aligned}\boldsymbol{E}(\boldsymbol{x},\omega) &= \exp(\mathrm{i}\boldsymbol{k}\cdot(\boldsymbol{x}-\boldsymbol{y})\mathbf{N}(\omega))\boldsymbol{E}(\boldsymbol{y},\omega)\\ &= \mathbf{T}(\boldsymbol{x}-\boldsymbol{y},\omega)\boldsymbol{E}(\boldsymbol{y},\omega),\end{aligned} \tag{46}$$

where the index of refraction $\mathbf{N} = 1 + 2\pi\bar{\boldsymbol{\chi}}$ was introduced. Equation (46) relates the electric field at two positions inside the material using the transmission function $\mathbf{T}$. The electric field is also transverse throughout the medium, i.e., $\boldsymbol{k}\cdot\boldsymbol{E} = 0$.

The index of refraction and the transmission function are second-rank tensors in normal space. However, the transversality of the electric field permits us to treat them like second-rank tensors in the two-dimensional subspace defined by the plane normal to $\boldsymbol{s}$, the propagation direction of the x-rays. The projection of the index of refraction into this subspace, $\mathbf{n}$, has a unique decomposition in terms of the three Pauli spin matrices:

$$\mathbf{n} = (1-\boldsymbol{s}\otimes\boldsymbol{s})\mathbf{N}(1-\boldsymbol{s}\otimes\boldsymbol{s}) = \mathrm{tr}(\mathbf{n}) + \sum_{j=1}^{3} a_j\boldsymbol{\sigma}_j, \tag{47}$$

where the coefficients a_j depend on the traceless part of $\mathbf{n}$ only. With this expansion and the use of the properties of the Pauli spin matrices, the transmission function may be converted to a form suitable for further discussion:

$$\mathbf{T} = \mathrm{e}^{\mathrm{i}\phi n}\left(\cos\phi\xi + \mathrm{i}\frac{\sin\phi\xi}{\xi}(\mathbf{n}-n)\right), \tag{48}$$

with

$$n = \tfrac{1}{2}\,\mathrm{tr}(\mathbf{n}), \qquad \phi = \boldsymbol{k}\cdot(\boldsymbol{x}-\boldsymbol{y}), \qquad \xi = \sqrt{n^2 - \det(\mathbf{n})}. \tag{49}$$

The non-resonant contributions from electronic charge to the index of refraction are isotropic and are included in n. The transmission function given in the form of (48) gives a full description of coherent elastic forward scattering of x-rays including optical activity and resonant behaviour.

Nuclear resonant contribution. The nuclear contribution to the index of refraction can be derived from the forward-scattering amplitude. From the formulae of [94] one obtains for the resonant part

$$\mathbf{n}(\omega) - 1 = \frac{c}{2\omega}\rho\sigma f\sum_{mm'}\frac{\mathbf{W}_{mm'}(\boldsymbol{s})}{z_{mm'}(\omega)-\mathrm{i}}, \tag{50}$$

where ρ is the volume density of resonant nuclei, σ is the nuclear resonant cross section, and f is the Lamb–Mössbauer factor. The sum is over all sublevels of nuclear ground and excited states. The function $z_{mm'} = 2\hbar(\omega_{mm'}-\omega)/\Gamma$ depends on the energy difference between excited and ground states $\hbar\omega_{mm'}$ and the nuclear level width Γ. The weight of each resonance at $\hbar\omega_{mm'}$ is given by the second-rank tensor $\mathbf{W}_{mm'}$. The weights are normalized by $\sum_{mm'}\mathbf{W}_{mm'} = 1$. In figure 11, a schematic diagram of the nuclear ground and excited states is shown for ^{57}Fe in the presence of a magnetic field. Here the weights take the simple form

$$\mathbf{W}_{m,m+M}(\boldsymbol{s}) = \frac{8\pi}{3}C^2(II'1;-mm+M)\boldsymbol{Y}^{(0)}_{1M}(\boldsymbol{s})\otimes\boldsymbol{Y}^{(0)*}_{1M}(\boldsymbol{s}), \tag{51}$$

where I, I' are spin quantum numbers of the nuclear ground and excited states, respectively, $\boldsymbol{Y}^{(0)}_{1M}$ gives the vector spherical harmonic representing the M1 multipole transition of ^{57}Fe, and $C(\cdots)$ are Clebsch–Gordan coefficients in the notation of Rose [95]. Let $\{\boldsymbol{p}_\sigma, \boldsymbol{p}_\pi, \boldsymbol{s}\}$ be an orthonormal basis in normal space. The x-rays are propagating along $\boldsymbol{s}$, and the other basis

vectors give the two possible directions of linear polarization. The representation of the vector spherical harmonics in this basis is then

$$\begin{aligned}
\boldsymbol{Y}^{(0)}_{11}(\boldsymbol{s}) &= \sqrt{\frac{3}{16\pi}}\{\boldsymbol{p}_\sigma(-\cos\varphi + \mathrm{i}\sin\varphi\cos\theta) - \boldsymbol{p}_\pi(\sin\varphi + \mathrm{i}\cos\varphi\cos\theta)\},\\
\boldsymbol{Y}^{(0)}_{10}(\boldsymbol{s}) &= \mathrm{i}\sqrt{\frac{3}{8\pi}}\sin\theta\{\boldsymbol{p}_\sigma\sin\varphi - \boldsymbol{p}_\pi\cos\varphi\},\\
\boldsymbol{Y}^{(0)}_{1,-1}(\boldsymbol{s}) &= \sqrt{\frac{3}{16\pi}}\{\boldsymbol{p}_\sigma(\cos\varphi + \mathrm{i}\sin\varphi\cos\theta) + \boldsymbol{p}_\pi(\sin\varphi - \mathrm{i}\cos\varphi\cos\theta)\},
\end{aligned} \tag{52}$$

where the angles θ and φ determine the direction of the magnetic field. If $\boldsymbol{b}$ is a unit vector giving the direction of the magnetic field, the angles are defined by $\cos\varphi\sin\theta = \boldsymbol{b}\cdot\boldsymbol{p}_\sigma$, $\sin\varphi\sin\theta = \boldsymbol{b}\cdot\boldsymbol{p}_\pi$, and $\cos\theta = \boldsymbol{b}\cdot\boldsymbol{s}$.

Thin-absorber approximation. The primary application of SMS is the determination of hyperfine interaction parameters. Effects related to the thickness of the sample lead to interesting phenomena [96–98] that have to be considered but, for spectroscopic measurements, are mostly unwanted. To understand more easily the influence of magnetic fields, as shown in figure 11, and of electric field gradients on time spectra, we will use (48) in the limit of thin absorbers. Assume the x-rays are transmitted through a platelet of thickness D. Then the geometrical phase takes the form $\phi = 2\pi D/\lambda$, where λ is the x-ray wavelength. We also apply the approximation $|(n-1)\phi| \ll 1$ to (48) and obtain the simplified expression

$$\mathsf{T} = \mathrm{e}^{\mathrm{i}\phi n_\mathrm{e}}(1 + \mathrm{i}\phi(\mathsf{n} - 1)), \tag{53}$$

where n_e are the non-resonant (electronic and vacuum) contributions to the index of refraction. Inspection of (50) shows that our approximation is justified if $\eta = \rho\sigma f D \ll 1$. The quantity η is called the 'effective thickness' of the platelet and is important for estimating thickness effects in SMS.

5.4. Time spectra

We now turn to a discussion of the transmitted intensity, which is the usual result of an experiment. First we need a satisfactory model for the radiation field that is incident on the sample. The x-rays emitted by the present SR sources can be understood as an incoherent superposition of one-photon fields. This does not change on employment of crystal optics for monochromatization, and the individual one-photon fields will henceforth be called 'SR components'. We then apply the transmission function to each SR component and perform an incoherent average over their individual properties to calculate intensities. For each SR component, the coherence length for all directions in space is much larger than the size of the nucleus. This is caused by a large distance between the nucleus and SR source, as well as by the monochromatization process. In addition, we will assume that the transverse coherence length of the SR components is larger than the typical dimension of the averaging volume that led us to (45). The incident field may then be represented by a plane quasimonochromatic wave with wavevector $\boldsymbol{k}$, average energy $\bar{\omega} = c|\boldsymbol{k}|$, and a time-dependent amplitude, i.e., $\boldsymbol{E}(\boldsymbol{y}, t) = \boldsymbol{p}_\sigma a(t)\exp(\mathrm{i}\boldsymbol{k}\cdot\boldsymbol{y} - \mathrm{i}\bar{\omega}t)$. The unit vector $\boldsymbol{p}_\sigma$ gives the time-independent polarization of the SR component. The function $a(t)$ describes the pulse structure of the SR component, as well as its energy spectrum including the modification by crystal optics. We assume that $a(t) = 0$ outside the time interval $[t_0, t_0 + \delta t]$, i.e., the SR component arrives at time t_0 at the sample and has a duration δt. The duration is much smaller than the nuclear lifetime and the inverse of the typical nuclear level splitting. The set $\{\boldsymbol{k}, \boldsymbol{p}_\sigma, a(t)\}$ presents a unique description

of the SR component. The contribution of the SR component to the intensity per time, after it passed through the resonant material, is given by

$$\frac{\mathrm{d}I}{\mathrm{d}t} = \left| \int R_{\sigma\sigma}(t-t')a(t')\,\mathrm{d}t' \right|^2 + \left| \int R_{\pi\sigma}(t-t')a(t')\,\mathrm{d}t' \right|^2. \tag{54}$$

Here $R_{\sigma\sigma}$ and $R_{\pi\sigma}$ are elements of the response function tensor $\mathbf{R}$. The second term describes the conversion of incident σ-polarized SR, a result of optical activity. The tensor $\mathbf{R}$ is related to the transmission function of (48) by Fourier transformation:

$$\mathbf{R}(t) = \int \mathbf{T}(\omega)\mathrm{e}^{-\mathrm{i}\omega t}\,\frac{\mathrm{d}\omega}{2\pi}. \tag{55}$$

In the thin-absorber limit, we can calculate the response function from (53) and (50). As required by causality, the response function vanishes for $t < 0$. For positive times $t \geqslant 0$ we obtain

$$\mathrm{e}^{-\mathrm{i}\phi n_\mathrm{e}}\mathbf{R}(t) = \delta(t) + \exp\left(-\frac{t}{2\tau}\right)\frac{\eta}{4\tau}\sum_j \mathbf{W}_j(\boldsymbol{s})\mathrm{e}^{-\mathrm{i}\omega_j t}, \tag{56}$$

where η is the effective thickness of the platelet, and $\tau = \hbar/\Gamma$ is the lifetime of the excited nuclear state. The index j comprises the two indices mm' of (50). Typically the duration of the SR pulse is much shorter than the lifetime τ which permits us to simplify (54) into the following form for the delayed intensity per time and $t \geqslant 0$:

$$\frac{\mathrm{d}I}{\mathrm{d}t} = I_0\frac{\eta^2}{16\tau}\exp(-t/\tau)\sum_{lj}\boldsymbol{p}_\sigma\mathbf{W}_l^\dagger\mathbf{W}_j\boldsymbol{p}_\sigma\mathrm{e}^{-\mathrm{i}(\omega_j-\omega_l)t}. \tag{57}$$

Here $I_0 = \exp(-2Dn_\mathrm{e}'')\Gamma|\int a(t)\,\mathrm{d}t|^2$ is the intensity incident into an energy bandwidth of Γ attenuated by electronic absorption in the platelet given by the imaginary part n_e'' of the non-resonant index of refraction. The delayed intensity constitutes the time spectrum, and, from a thin platelet, we calculate an exponential decay with the natural lifetime. Superimposed on the decay are oscillations caused by the nuclear level splitting. To illustrate this point, we will consider several special cases. First the trivial case of vanishing magnetic field, i.e., where all values ω_j are the same. Using the normalization of the weight tensor $\mathbf{W}$, we immediately obtain $\mathrm{d}I/\mathrm{d}t \propto \exp(-t/\tau)$, i.e., no oscillations, just natural decay.

Oscillations from magnetic fields. Figure 14 displays measured time spectra of a magnetized foil of ^{57}Fe. In panel (a), the direction of the magnetic field is perpendicular to both the direction and the polarization of the incident SR, i.e., in the direction of $\boldsymbol{p}_\pi$. This corresponds to $\theta = \pi/2$ and $\varphi = \pi/2$ in (52). The incident SR was σ polarized, and therefore the only relevant components of the weight tensors are

$$\boldsymbol{p}_\sigma\mathbf{W}_{mm}\boldsymbol{p}_\sigma = C^2(II'1;-mm). \tag{58}$$

This means that only the $-1/2 \to -1/2$ and the $1/2 \to 1/2$ transitions will contribute to the time spectrum, and from (57) we obtain

$$\frac{\mathrm{d}I}{\mathrm{d}t} = I_0\frac{\eta^2}{16\tau}\exp(-t/\tau)\cos^2\omega t, \tag{59}$$

where $\hbar\omega = B(\mu_\mathrm{g} - \mu_\mathrm{e}/3)$ is half the difference of the $-1/2 \to -1/2$ and $1/2 \to 1/2$ transition energies, which were substituted according to (40). We expect the time spectrum to show a single oscillation frequency, which is nicely confirmed by the data in figure 14(a). The dashed curve was obtained with (59) and values of $\tau = 46$ ns and $2\pi/\omega = 28.2$ ns. The reduced value for τ is a thickness effect caused by the rather large effective thickness of

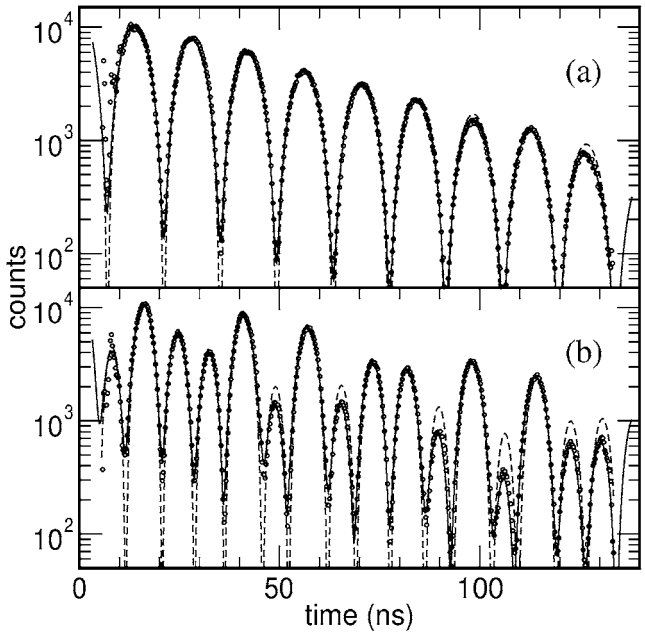

Figure 14. Time spectra of an iron foil. In panel (a), the direction of the magnetic field is perpendicular to the direction and the polarization of the incident SR. In panel (b), the direction of the magnetic field is parallel to the polarization of the incident SR. The circles show measured data, and the solid curves are calculations with the CONUSS software [84] including thickness effects and slight misorientations of the samples. The dashed curves are calculations according to (59) for case (a) and according to (61) for case (b).

$\eta = 20$, which corresponds to an about 1.3 μm thick iron foil fully enriched in ^{57}Fe. From the oscillation frequency, we obtain $B = 32.6$ T in excellent agreement with expectation.

Panel (b) of figure 14 shows a more complicated oscillation pattern. In this case, the direction of the magnetic field is parallel to the direction of the polarization of the incident SR, i.e., in the direction of $\boldsymbol{p}_\sigma$ corresponding to $\theta = \pi/2$ and $\varphi = 0$ in (52). Now there are four components of the weight tensors that have to be considered:

$$\boldsymbol{p}_\sigma \mathbf{W}_{m,m\pm1} \boldsymbol{p}_\sigma = \tfrac{1}{2} C^2 (I I' 1; -m m \pm 1). \tag{60}$$

The transitions $-1/2 \to 1/2$ and $1/2 \to -1/2$ contribute with a weight of $1/8$, and, for the $-1/2 \to -3/2$ and $1/2 \to 3/2$ transitions, we calculate weights of $3/8$. The time spectrum is given by

$$\frac{\mathrm{d}I}{\mathrm{d}t} = I_0 \frac{\eta^2}{16\tau} \exp(-t/\tau) \left(\frac{3}{4} \cos \omega_1 t + \frac{1}{4} \cos \omega_2 t \right)^2, \tag{61}$$

where $\hbar\omega_1 = B(\mu_\mathrm{g} - \mu_\mathrm{e})$ is half the difference of the $-1/2 \to -3/2$ and $1/2 \to 3/2$ transition energies, and $\hbar\omega_2 = B(\mu_\mathrm{g} + \mu_\mathrm{e}/3)$ is half the difference of the $-1/2 \to 1/2$ and $1/2 \to -1/2$ transition energies. The fact that two frequencies modulate the nuclear decay leads to a more complicated time spectrum than before. This can be seen in figure 14(b). The dashed curve was obtained with (61) and values of $\tau = 59$ ns, $2\pi/\omega_1 = 16.4$ ns, and $2\pi/\omega_1 = 103$ ns. As before, the reduced value for τ is a thickness-related effect, and, from the oscillation frequencies, we again obtain $B = 32.6$ T.

Oscillations from electric field gradients. An axially symmetric electric field gradient represents a higher symmetry than the case of a magnetic field, and we can use (51) to calculate the index of refraction. The nuclear level splitting was given in (39), and for the ^{57}Fe isotope we find two groups of nuclear transitions, $\pm 1/2 \rightarrow \pm 1/2$ and $-1/2 \rightarrow -3/2$, $1/2 \rightarrow 3/2$. We will now calculate time spectra for the efg axis along the directions $\boldsymbol{p}_\sigma$, $\boldsymbol{p}_\pi$, $\boldsymbol{s}$, where we assume as previously that the incident SR is σ polarized. For the efg axis parallel to $\boldsymbol{p}_\sigma$, the $-1/2 \rightarrow 1/2$ and $1/2 \rightarrow -1/2$ transitions contribute, and we calculate the weights

$$\boldsymbol{p}_\sigma(\mathbf{W}_{1/2,-1/2} + \mathbf{W}_{-1/2,1/2})\boldsymbol{p}_\sigma = C^2(II'1;\, 1/2\; 1/2) = \tfrac{1}{4}. \tag{62}$$

For the $-1/2 \rightarrow -3/2$ and $1/2 \rightarrow 3/2$ transitions, the weights are

$$\boldsymbol{p}_\sigma(\mathbf{W}_{-1/2,-3/2} + \mathbf{W}_{1/2,3/2})\boldsymbol{p}_\sigma = C^2(II'1;\, 1/2\; -3/2) = \tfrac{3}{4}. \tag{63}$$

The calculated time spectrum is then given by

$$\frac{\mathrm{d}I}{\mathrm{d}t} = I_0 \frac{\eta^2}{16\tau} \exp(-t/\tau)\left(\frac{3}{4}\cos^2 \omega t + \frac{1}{4}\right), \tag{64}$$

where $\hbar\omega = \Delta/2$ is half the difference of the transition energies. The time spectrum is modulated with an oscillation that directly gives the quadrupole splitting introduced in (39). We also note that, in contrast to the examples with magnetic field, the time spectrum has no zero intensities, i.e., the modulation index is only 75%.

If the efg axis is parallel to $\boldsymbol{p}_\pi$, only $-1/2 \rightarrow -1/2$ and $1/2 \rightarrow 1/2$ have non-vanishing weights:

$$\boldsymbol{p}_\sigma(\mathbf{W}_{-1/2,-1/2} + \mathbf{W}_{1/2,1/2})\boldsymbol{p}_\sigma = 2C^2(II'1;\, 1/2\; -1/2) = 1. \tag{65}$$

The time spectrum shows no oscillations:

$$\frac{\mathrm{d}I}{\mathrm{d}t} = I_0 \frac{\eta^2}{16\tau} \exp(-t/\tau), \tag{66}$$

even though we have a non-zero nuclear level splitting. The oscillations are suppressed by virtue of the selection rules in combination with the specific orientation of the efg axis relative to the linearly polarized SR.

Finally, we consider the case in which the efg axis is parallel to $\boldsymbol{s}$, the propagation direction of the SR. The contributing transitions and the corresponding weights are identical to the case with the efg axis parallel to $\boldsymbol{p}_\sigma$. The time spectrum is then given by (64).

In many applications, the sample is a conglomerate of small crystallites that are randomly oriented. The time spectrum of such an absorber can be calculated by adding all the above contributions from orthogonal efg axes coherently. Now the $\pm 1/2 \rightarrow \pm 1/2$ transitions add up to a weight of $1/4 + 1 + 1/4 = 3/2$, and the $-1/2 \rightarrow -3/2$, $1/2 \rightarrow 3/2$ transitions give $3/4 + 0 + 3/4 = 3/2$. The time spectrum takes the form

$$\frac{\mathrm{d}I}{\mathrm{d}t} = I_0 \frac{\eta^2}{16\tau} \exp(-t/\tau)\cos^2 \omega t, \tag{67}$$

where the oscillation frequency is given by $\hbar\omega = \Delta/2$, identical to that in (64). Interestingly the modulation index is now increased to 100%, which is possible in a coherent averaging process. If a reduced modulation index is observed in a time spectrum of such a conglomerate, it is therefore possible that a texture is present, i.e., some preferred orientation of crystallites exists.

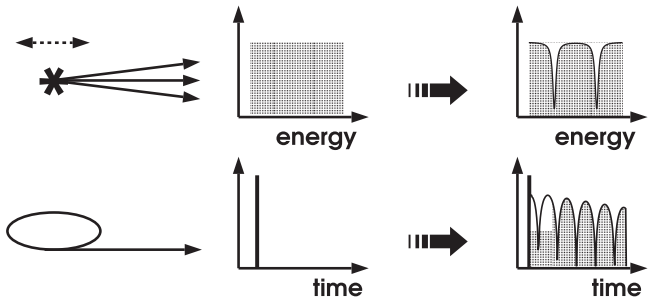

Figure 15. Reciprocal properties of radioactive sources (top) and SR (bottom) lead to reciprocal experimental techniques. The centre panels illustrate the source characteristics averaged over a time period needed for data collection. The panels on the right show the typical spectra obtained with either technique.

Table 2. Comparison between a modern SR source and a commercially available ^{57}Co source with 100 mCi activity. The SR data includes losses in x-ray optics. Energy resolution and energy range depend of the measurement technique as explained in the text. They are given for completeness only. Spectral flux is given in units of photons s^{-1} eV^{-1}, brightness in units of photons s^{-1} eV^{-1} sr^{-1}, and spectral flux density in units of photons s^{-1} eV^{-1} mm^{-2}.

Property	SR	^{57}Co source
Spectral flux	3×10^{12}	2.5×10^{10}
Brightness	1×10^{22}	2.5×10^{13}
Spectral flux density	5×10^{12}	2×10^{5}
(Focused)	2×10^{16}	—
Typical beam size (mm^2)	0.4×2	10×10
Focused beam size (μm^2)	6×6	—
Polarization	Linear or circular	Unpolarized
Best energy resolution (eV)	4.7×10^{-9}	9.4×10^{-9}
Energy range (eV)	$\approx 8 \times 10^{-5}$	$\approx 1 \times 10^{-4}$

6. Radiation sources for NRS

A comparison of SMS with more traditional methods of Mössbauer spectroscopy reduces to an evaluation of properties of the radiation sources used. Synchrotron radiation and γ-rays emitted by a radioactive source have very different properties. However, both types of source permit Mössbauer experiments aiming at extraction of hyperfine parameters. The SR is emitted in short intense pulses that repeat periodically. In contrast, the emission of photons from a radioactive nucleus is random in time. The situation is inverted if we analyse the energy bandwidth for both sources, which is of the order of keV for the SR but only about the natural linewidth for a Mössbauer source. This reciprocal behaviour prompts the conclusion that the experimental techniques should be similarly reciprocal, i.e., energy-resolved spectroscopy with radioactive sources and time-resolved spectroscopy with SR, as illustrated in figure 15. Table 2 summarizes the results of our quantitative source comparison.

6.1. X-ray flux densities

A fair comparison of the relevant intensity provided by either source has to consider the particular method of measurement, i.e., energy resolved or time resolved. A commercially

available ^{57}Co source with 100 mCi activity produces an equivalent spectral photon flux of approximately 2.5×10^{10} photons s^{-1} eV^{-1} into 2×2 deg^2 solid angle (0.001 sr) if the range of the measurement covers 200 natural linewidths. Including losses in the optical elements, the undulator beamline 3-ID at the Advanced Photon Source provides about 3×10^9 photons s^{-1} in a 1 meV bandwidth onto the sample. This leads to a spectral flux of 3×10^{12} photons s^{-1} eV^{-1} into 0.0005×0.002 deg^2 solid angle (3×10^{-10} sr). If samples are small and only accept radiation in a small spatial or angular range, it is particularly useful to know the brightness (spectral flux per solid angle) and spectral flux density (spectral flux per area) of the source. For the radioactive source, we obtain a brightness of 2.5×10^{13} photons s^{-1} eV^{-1} sr^{-1} and, at 10 cm distance, a spectral flux density of 2×10^5 photons s^{-1} eV^{-1} mm^{-2}. As perhaps expected, SR source achieves much higher values providing a brightness of 10^{22} photons s^{-1} eV^{-1} sr^{-1} and a spectral flux density of 5×10^{12} photons s^{-1} eV^{-1} mm^{-2} at 35 m distance from the source. Elliptically bent mirrors allow focusing of the x-ray beam to about 6×6 μm^2 spot size. This increases the spectral flux density to 2×10^{16} photons s^{-1} eV^{-1} mm^{-2}.

The high flux densities of SR are of particular importance if samples are small. In experiments under Mbar pressures using diamond anvil cells [38], the sample diameter is typically less than 50 μm. Even if the radioactive source is moved as close as 1 cm, the spectral photon flux on the sample is still seven orders of magnitude smaller than for the focused SR.

6.2. Energy resolution

Other important characteristics are the best resolution obtainable and the maximum range achievable. The energy bandwidth of the radioactive source is given by the natural linewidth, and this leads to an optimum resolution in conventional Mössbauer spectroscopy of 2Γ. The maximum energy range obtained by Doppler-shifting techniques is typically 10^{-4} eV. In the case of SR, we have to analyse the situation with respect to a time-resolved measurement. The energy resolution δE relates to the recorded period of time δt following the excitation of the sample by a flash of SR. We obtain from [99]

$$\delta E = \Gamma \coth\left(\frac{\Gamma\,\delta t}{4\hbar}\right). \tag{68}$$

The time period is given by the bunch separation minus the detector dead time and is therefore subject to the operational mode of the storage ring and detector quality. The energy resolution of the radioactive source is exceeded if $\delta t > 2.2\hbar/\Gamma$. The optimal resolution is given by $\delta E = \Gamma$. The maximum energy range that is probed by the time spectrum follows from the time resolution of the detector; present best values are about 100 ps [100]. Figure 14(b) shows oscillations with a period of 16.4 ns, which correspond to a difference in nuclear transition energies of 0.5 μeV. Assuming that the largest energy difference observable produces oscillations with a 100 ps period, we obtain 83 μeV. Energy ranges of SMS and conventional Mössbauer spectroscopy are comparable, but the achievable energy resolution for SMS strongly depends on the bunch separation.

6.3. Polarization

The polarization of the emitted radiation is an important property of the source. Essentially all applications of conventional Mössbauer spectroscopy use radioactive sources that emit unpolarized radiation. The mechanism producing SR guarantees almost complete linear polarization. In addition, optical elements can convert SR to circularly polarized radiation with

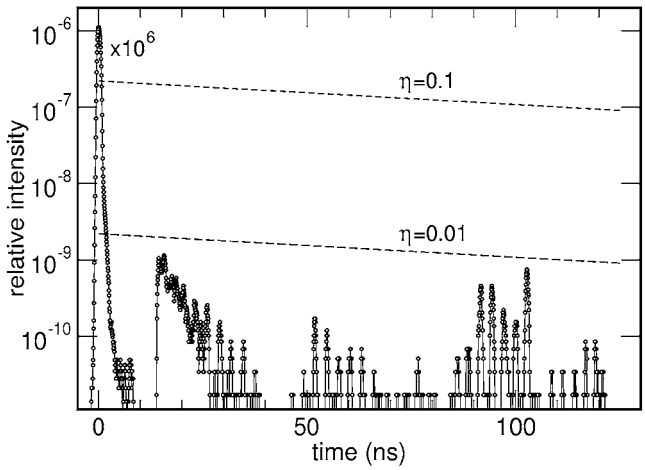

Figure 16. Bunch purity typical for the Advanced Photon Source. Intensities are given relative to the main bunch, which is shown at zero time with reduced height. The dashed lines correspond to nuclear delayed intensities for the indicated values of the effective sample thickness and were calculated using (57).

high efficiency [101]. Control over the polarization of the source is of particular importance for investigations of magnetic field directions in nanostructures [19].

6.4. Bunch purity

All NRS experiments collect delayed events that are registered between the x-ray pulses. The sensitivity of a particular experiment is therefore strongly dependent on the background between electron bunches. The process of filling the storage ring with electrons is usually very reliable but not perfect. The less the charge found between the main bunches, the larger the bunch purity. Figure 16 shows a time spectrum of the region between main bunches without nuclear scatterers in the x-ray path. The bunch purity is better than 10^{-9} for most of the interbunch region, but we can clearly identify weak bunches, so-called 'spurious bunches'. We also calculated nuclear forward scattering from (57) assuming no nuclear level splitting and different effective thicknesses. Clearly the sensitivity is sufficient to obtain spectra from samples as thin as $\eta = 0.01$, which corresponds to 0.63 nm or about five monolayers of ^{57}Fe metal. However, we note that disturbances from spurious bunches may become visible if samples either show strongly accelerated decay or exhibit nuclear level splittings leading to low-intensity regions in the time spectrum.

7. Outlook

On the preceding pages, we introduced two particular NRS techniques that are applied to a variety of problems in condensed-matter physics, material science, geophysics, biophysics, and chemistry. The NRIXS and SMS methods have prospered with the commissioning of third-generation SR sources. We expect even greater potential if the brilliance of these sources can be further increased by optimization of undulator technology or operating parameters of the storage ring. If fourth-generation sources (x-ray lasers) become a reality at sub-ångström wavelengths, orders of magnitude increases in spectral flux density can be expected with tremendous opportunities for 'flux-hungry' NRS and inelastic x-ray scattering techniques.

Besides the NRS techniques that were discussed in this paper, there are interesting developments that may become more widely used in the future. The 'nuclear lighthouse effect' (NLE) occurs in rotating samples that also show coherent NRS [102]. The NLE permits mapping of the decay of resonantly excited nuclei onto an angle scale and thus achievement of excellent time resolution independently of the time structure of the SR [103, 104].

In many cases, the interpretation of time spectra as they are collected in SMS is less intuitive than that of energy spectra. This issue was partially addressed by a time-integrated method that uses Doppler-shifted standard absorbers in addition to the sample [105–107]. Another approach tries to determine the phase of the transmitted time-dependent x-ray field and then to reconstruct the energy spectrum by Fourier transformation [99, 108]. The advantage of these approaches is the simplification of the spectrum, however, at the expense of a more sophisticated experimental set-up and longer data collection times.

NRS has also been used as a means of energy analysis in the millielectronvolt regime [109] and as a filtering technique for resolving quasielastic scattering in the nanoelectronvolts–microelectronvolts regime [110]. In both cases, the samples investigated do not contain resonant nuclei. Another approach used polarization filtering of resonantly scattered x-rays [111, 112] to prepare microelectronvolt bandwidth radiation. Attempts were made to use such radiation to perform NRIXS experiments [113]. At present, the application of these ultrahigh-resolution techniques is mostly hampered by the often insufficient photon flux.

The excellent reproducibility and the narrow energy width of the 14.4125 keV transition of ^{57}Fe led to a proposal to use nuclear transitions as wavelength standards in the x-ray regime [114, 115]. This approach seems very promising, in particular if the accuracy can be improved beyond the present 0.2 ppm, e.g., by direct comparison of a nuclear resonant wavelength to laser light emission.

In summary, there can be little doubt that x-ray spectroscopies with SR are a growing area of research with a special role for NRS methods, such as NRIXS and SMS.

Acknowledgments

I am grateful to T S Toellner for valuable discussions. This work was supported by the US Department of Energy, Basic Energy Sciences, Office of Science, under Contract No W-31-109-Eng-38.

References

[1] Gerdau E and de Waard H (ed) 1999/2000 *Nuclear Resonant Scattering of Synchrotron Radiation; Hyperfine Interact.* **123–125**
[2] Gerdau E, Rüffer R, Winkler H, Tolksdorf W, Klages C P and Hannon J P 1985 *Phys. Rev. Lett.* **54** 835
[3] Ruby S L 1974 *J. Physique Coll.* **35** C6 209
[4] Nasu S 1994 *Hyperfine Interact.* **90** 59
Nasu S 1998 *Hyperfine Interact.* **113** 97
[5] Zhang L, Stanek J, Hafner S S, Ahsbahs H, Grünsteudel H F, Metge J and Rüffer R 1999 *Am. Mineral.* **84** 447
[6] Pleines M, Lübbers R, Strecker M, Wortmann G, Leupold O, Shvyd'ko Y V, Gerdau E and Metge J 1999 *Hyperfine Interact.* **120/121** 181
[7] Lübbers R, Wortmann G and Grünsteudel H F 1999 *Hyperfine Interact.* **123/124** 529
[8] Kobayashi H, Yoda Y and Kamimura T 1999 *Japan. J. Appl. Phys.* **38-1** 409
[9] Toellner T S, Sturhahn W, Alp E E, Röhlsberger R, Sowers C H and Fullerton E E 1995 *Phys. Rev. Lett.* **74** 3475
[10] Nagy D L, Bottyán L, Deák L and Szilágyi E 1997 *Balkan Phys. Lett.* **5** 240
[11] Niesen B, Rosu M F, Mugarza A, Coehoorn R, Jungblut R M, Rooseboom F, Baron A Q R, Chumakov A I and Rüffer R 1998 *Phys. Rev.* B **58** 8590
[12] Bottyán L, Dekoster J, Deák L, Baron A Q R, Degroote S, Moons R, Nagy D L and Langouche G 1998 *Hyperfine Interact.* **113** 295
[13] Chumakov A I, Niesen L, Nagy D L and Alp E E 1999 *Hyperfine Interact.* **123/124** 427

[14] Röhlsberger R 1999 *Hyperfine Interact.* **123/124** 455
[15] Kobayashi H, Nasu S, Nakamichi T, Sato M and Seto M 1999 *Japan. J. Appl. Phys.* **38-1** 412
[16] Dekoster J *et al* 2000 *Hyperfine Interact.* **126** 349
[17] Nagy D L, Bottyán L, Deák L, Szilágyi E, Spiering H, Dekoster J and Langouche G 2000 *Hyperfine Interact.* **126** 353
[18] Röhlsberger R, Bansmann J, Senz V, Bettac A, Jonas K L, Leupold O, Rüffer R, Burkel E and Meiwes-Broer K H 2001 *Phys. Rev. Lett.* **86** 5597
[19] Röhlsberger R, Thomas H, Schlage K, Burkel E, Leupold O and Rüffer R 2002 *Phys. Rev. Lett.* **89** 237201
[20] Senz V, Röhlsberger R, Bansmann J, Leupold O and Meiwes-Broer K H 2003 *New J. Phys.* **5** 47.1
[21] Winkler H, Leupold O, Grünsteudel H, Meyer W, Grünsteudel H F, Realo E, Trautwein A X, Gerdau E, Mandon D and Weiss R 1995 *J. Inorg. Biochem.* **59** 327
[22] Haas M, Realo E, Winkler H, Meyer-Klaucke W, Trautwein A X, Leupold O and Rüter H-D 1997 *Phys. Rev.* B **56** 14082
[23] Trautwein A X *et al* 1998 *Pure Appl. Chem.* **70** 917
[24] Trautwein A X and Winkler H 1999 *Hyperfine Interact.* **123/124** 561
[25] Leupold O and Winkler H 1999 *Hyperfine Interact.* **123/124** 571
[26] Haas M, Realo E, Winkler H, Meyer-Klaucke W, Trautwein A X and Leupold O 2000 *Phys. Rev.* B **61** 4155
[27] Keppler C, Achterhold K, Ostermann A, van Bürck U, Chumakov A I, Rüffer R, Sturhahn W, Alp E E and Parak F 2000 *Eur. Biophys. J.* **29** 146
[28] Visscher W M 1960 *Ann. Phys.* **9** 194
[29] Singwi K S and Sjölander A 1960 *Phys. Rev.* **120** 1093
[30] Weiss H and Langhoff H 1979 *Phys. Lett.* A **69** 448
Weiss H and Langhoff H 1979 *Z. Phys.* B **33** 365
[31] Endres G, Strohkendl F, Langhoff H and Gmelin F 1981 *Z. Phys.* B **44** 253
[32] Seto M, Yoda Y, Kikuta S, Zhang X W and Ando M 1995 *Phys. Rev. Lett.* **74** 3828
[33] Sturhahn W, Toellner T S, Alp E E, Zhang X W, Ando M, Yoda Y, Kikuta S, Seto M, Kimball C W and Dabrowski B 1995 *Phys. Rev. Lett.* **74** 3832
[34] Chumakov A I, Rüffer R, Grünsteudel H, Grünsteudel H F, Grübel G, Metge J and Goodwin H A 1995 *Europhys. Lett.* **30** 427
[35] Kohn V G, Chumakov A I and Rüffer R 1998 *Phys. Rev.* B **58** 8437
[36] Sturhahn W and Kohn V G 1999 *Hyperfine Interact.* **123/124** 367
[37] Lübbers R, Grünsteudel H F, Chumakov A I and Wortmann G 2000 *Science* **287** 1250
[38] Mao H K *et al* 2001 *Science* **292** 914
[39] Struzhkin V V *et al* 2001 *Phys. Rev. Lett.* **87** 255501
[40] Giefers H, Lübbers R, Rupprecht K, Wortmann G, Alfè D and Chumakov A I 2002 *High Pressure Res.* **22** 501
[41] Paulsen H, Winkler H, Trautwein A X, Grünsteudel H, Rusanov V and Toftlund H 1999 *Phys. Rev.* B **59** 975
[42] Paulsen H, Benda R, Herta C, Schünemann V, Chumakov A I, Duelund L, Winkler H, Toftlund H and Trautwein A X 2001 *Phys. Rev. Lett.* **86** 1351
[43] Sage J T, Paxson C, Wyllie G R A, Sturhahn W, Durbin S M, Champion P M, Alp E E and Scheidt W R 2001 *J. Phys.: Condens. Matter* **13** 7707
[44] Rai B K, Durbin S M, Prohofsky E W, Sage J T, Wyllie G R A, Scheidt W R, Sturhahn W and Alp E E 2002 *Biophys. J.* **82** 2951
[45] Rai B K, Durbin S M, Prohofsky E W, Sage J T, Wyllie G R A, Ellison M K, Scheidt W R, Sturhahn W and Alp E E 2002 *Phys. Rev.* E **66** 051904
[46] Achterhold K *et al* 1996 *Eur. Biophys. J.* **25** 43
[47] Keppler C, Achterhold K, Ostermann A, van Bürck U, Potzel W, Chumakov A I, Baron A Q R, Rüffer R and Parak F 1997 *Eur. Biophys. J.* **25** 221
[48] Parak F and Achterhold K 1999 *Hyperfine Interact.* **123/124** 825
[49] Sage J T, Durbin S M, Sturhahn W, Wharton D C, Champion P M, Hession P, Sutter J and Alp E E 2001 *Phys. Rev. Lett.* **86** 4966
[50] Achterhold K, Keppler C, Ostermann A, van Bürck U, Sturhahn W, Alp E E and Parak F 2002 *Phys. Rev.* E **65** 051916
[51] Röhlsberger R, Sturhahn W, Toellner T S, Quast K W, Alp E E, Bernhard A, Metge J, Rüffer R and Burkel E 1999 *Physica* B **263/264** 581
[52] Sturhahn W, Röhlsberger R, Alp E E, Ruckert T, Schrör H and Keune W 1999 *J. Magn. Magn. Mater.* **198/199** 590
[53] Röhlsberger R, Sturhahn W, Toellner T S, Quast K W, Hession P, Hu M, Sutter J and Alp E E 1999 *J. Appl. Phys.* **86** 584

[54] Keune W and Sturhahn W 1999 *Hyperfine Interact.* **123/124** 847
[55] Ruckert T, Keune W, Sturhahn W, Hu M Y, Sutter J P, Toellner T S and Alp E E 2000 *Hyperfine Interact.* **126** 363
[56] Roldan Cuenya B, Keune W, Sturhahn W, Toellner T S and Hu M Y 2001 *Phys. Rev.* B **64** 235321
[57] Ruckert T, Keune W, Sturhahn W and Alp E E 2002 *J. Magn. Magn. Mater.* **240** 562
[58] Fultz B, Ahn C C, Alp E E, Sturhahn W and Toellner T S 1997 *Phys. Rev. Lett.* **79** 937
[59] Seto M, Kobayashi K, Kitao S, Haruki R, Mitsui T, Yoda Y, Nasu S and Kikuta S 2002 *Phys. Rev.* B **61** 11425
[60] Pasquini L, Barla A, Chumakov A I, Leupold O, Rüffer R, Deriu A and Bonetti E 2002 *Phys. Rev.* B **66** 073410
[61] Tsunoda Y, Kurimoto Y, Seto M, Kitao S and Yoda Y 2002 *Phys. Rev.* B **66** 214304
[62] Fultz B, Stevens T A, Sturhahn W, Toellner T S and Alp E E 1998 *Phys. Rev. Lett.* **80** 3304
[63] Fultz B, Stevens T A, Alp E E, Hu M Y, Sutter J P, Toellner T S and Sturhahn W 2000 *Phys. Rev.* B **61** 14517
[64] Baron A Q R 2000 *Hyperfine Interact.* **125** 29
[65] Toellner T S 2000 *Hyperfine Interact.* **125** 3
[66] Toellner T S, Hu M Y, Sturhahn W, Bortel G, Alp E E and Zhao J 2001 *J. Synchrotron Radiat.* **8** 1082
[67] Chumakov A I, Baron A Q R, Arthur J, Ruby S L, Brown G S, Smirnov G V, van Bürck U and Wortmann G 1995 *Phys. Rev. Lett.* **75** 549
[68] Sturhahn W, Gerdau E, Hollatz R, Rüffer R, Rüter H-D and Tolksdorf W 1991 *Europhys. Lett.* **14** 821
[69] Johnson D E, Siddons D P, Larese J Z and Hastings J B 1995 *Phys. Rev.* B **51** 7909
[70] Leupold O, Pollmann J, Gerdau E, Rüter H-D, Faigel G, Tegze M, Bortel G, Rüffer R, Chumakov A I and Baron A Q R 1996 *Europhys. Lett.* **35** 671
[71] Kitao S, Mitsui T and Seto M 2000 *J. Phys. Soc. Japan* **69** 683
[72] Alp E E, Mooney T M, Toellner T, Sturhahn W, Witthoff E, Röhlsberger R and Gerdau E 1993 *Phys. Rev. Lett.* **70** 3351
[73] Koyama I, Yoda Y, Zhang X W, Ando M and Kikuta S 1996 *Japan. J. Appl. Phys.* **35** 6297
[74] Seto M, Kitao S, Kobayashi Y, Haruki R, Mitsui T, Yoda Y, Zhang X W and Maeda Yu 2000 *Phys. Rev. Lett.* **84** 566
[75] Sturhahn W and Toellner T S 2002 *Phys. Rev.* B **65** 134305
[76] Van Hove L 1954 *Phys. Rev.* **95** 249
[77] Mössbauer R L 1958 *Z. Phys.* **151** 124
[78] Sturhahn W and Chumakov A I 1999 *Hyperfine Interact.* **123/124** 809
[79] Mühlhaupt G and Rüffer R 1999 *Hyperfine Interact.* **123/124** 13
[80] Lipkin H J 1960 *Ann. Phys.* **9** 332
[81] Lipkin H J 1995 *Phys. Rev.* B **52** 10073
[82] Johnson D W and Spence J C H 1974 *J. Phys. D: Appl. Phys.* **7** 771
[83] Hu M Y, Sturhahn W, Toellner T S, Hession P M, Sutter J P and Alp E E 1999 *Nucl. Instrum. Methods* A **428** 551
[84] Sturhahn W 2000 *Hyperfine Interact.* **125** 149
[85] Kohn V G and Chumakov A I 2000 *Hyperfine Interact.* **125** 205
[86] Chumakov A I, Barla A, Rüffer R, Metge J, Grünsteudel H F, Grünsteudel H, Plessel J, Winkelmann H and Abd-Elmeguid M M 1998 *Phys. Rev.* B **58** 254
[87] Hu M Y, Sturhahn W, Toellner T S, Mannheim P D, Brown D E, Zhao J and Alp E E 2003 *Phys. Rev.* B **67** 094304
[88] Smirnov G V 1999 *Hyperfine Interact.* **123/124** 31
[89] Kagan Yu 1999 *Hyperfine Interact.* **123/124** 83
[90] Hannon J P and Trammell G T 1999 *Hyperfine Interact.* **123/124** 127
[91] Shvyd'ko Y V 1999 *Hyperfine Interact.* **123/124** 275
[92] Hastings J B, Siddons D P, van Bürck U, Hollatz R and Bergmann U 1991 *Phys. Rev. Lett.* **66** 770
[93] Blume M and Kistner O C 1968 *Phys. Rev.* **171** 417
[94] Sturhahn W and Gerdau E 1994 *Phys. Rev.* B **49** 9285
[95] Rose M E 1957 *Elementary Theory of Angular Momentum* (New York: Wiley)
[96] van Bürck U, Siddons D P, Hastings J B, Bergmann U and Hollatz R 1992 *Phys. Rev.* B **46** 6207
[97] Shvyd'ko Yu V, van Bürck U, Potzel W, Schindelmann P, Gerdau E, Leupold O, Metge J, Rüter H-D and Smirnov G V 1998 *Phys. Rev.* B **57** 3552
[98] Shvyd'ko Yu V and van Bürck 1999 *Hyperfine Interact.* **123/124** 511
[99] Sturhahn W 2001 *Phys. Rev.* B **63** 094105
[100] Kishimoto S 1998 *J. Synchrotron Radiat.* **5** 275
[101] Hirano K, Ishikawa T and Kikuta S 1993 *Nucl. Instrum. Methods* A **336** 343

[102] Röhlsberger R, Toellner T S, Sturhahn W, Quast K W, Alp E E, Bernhard A, Burkel E, Leupold O and Gerdau E 2000 *Phys. Rev. Lett.* **84** 1007
[103] Röhlsberger R, Quast K W, Toellner T S, Lee P L, Sturhahn W, Alp E E and Burkel E 2001 *Appl. Phys. Lett.* **78** 2970
[104] Röhlsberger R, Quast K W, Toellner T S, Lee P L, Sturhahn W, Alp E E and Burkel E 2001 *Phys. Rev. Lett.* **87** 047601
[105] L'abbé C, Coussement R, Odeurs J, Alp E E, Sturhahn W, Toellner T S and Johnson C 2000 *Phys. Rev.* B **61** 4181
[106] Callens R, Coussement R, Kawakami T, Ladriére, Nasu S, Ono T, Serdons I, Vyvey K, Yamada T and Odeurs J 2003 *Phys. Rev.* B **67** 104423
[107] Callens R, Coussement R, L'abbé C, Nasu S, Vyvey K, Yamada T, Yoda Y and Odeurs J 2003 *Phys. Rev.* B **65** 180404
[108] Sturhahn W, L'abbé C and Toellner T S 2003 Exo-interferometric phase determination of x-rays *Preprint* physics/0305038
[109] Chumakov A I, Baron A Q R, Rüffer R, Grünsteudel H, Grünsteudel H F and Meyer A 1996 *Phys. Rev. Lett.* **76** 4258
[110] Baron A Q R, Franz H, Meyer A, Rüffer R, Burkel E and Petry W 1997 *Phys. Rev. Lett.* **79** 2823
[111] Toellner T S, Alp E E, Sturhahn W, Zhang X W, Ando M, Yoda Y and Kikuta S 1995 *Appl. Phys. Lett.* **67** 1993
[112] Siddons D P, Hastings J B, Bergmann U, Sette F and Krisch M 1995 *Nucl. Instrum. Methods* B **103** 371
[113] Röhlsberger R, Gerdau E, Rüffer R, Sturhahn W, Toellner T S, Chumakov A I and Alp E E 1997 *Nucl. Instrum. Methods* A **394** 251
[114] Shvyd'ko Yu V *et al* 2000 *Phys. Rev. Lett.* **85** 495
[115] Shvyd'ko Yu V, Lucht M, Gerdau E, Lerche M, Alp E E, Sturhahn W, Sutter J and Toellner T S 2002 *J. Synchrotron Radiat.* **9** 17